



Calhoun: The NPS Institutional Archive
DSpace Repository

Theses and Dissertations

1. Thesis and Dissertation Collection, all items

2020-12

I-SPAR BUOY: DESIGN OF A LIGHTWEIGHT SHALLOW WATER AIR-SEA MEASUREMENT PLATFORM

Chamberlain, Vincent D., III

Monterey, CA; Naval Postgraduate School

<http://hdl.handle.net/10945/66607>

This publication is a work of the U.S. Government as defined in Title 17, United States Code, Section 101. Copyright protection is not available for this work in the United States.

Downloaded from NPS Archive: Calhoun



Calhoun is the Naval Postgraduate School's public access digital repository for research materials and institutional publications created by the NPS community. Calhoun is named for Professor of Mathematics Guy K. Calhoun, NPS's first appointed -- and published -- scholarly author.

Dudley Knox Library / Naval Postgraduate School
411 Dyer Road / 1 University Circle
Monterey, California USA 93943

<http://www.nps.edu/library>



NAVAL POSTGRADUATE SCHOOL

MONTEREY, CALIFORNIA

THESIS

**I-SPAR BUOY:
DESIGN OF A LIGHTWEIGHT SHALLOW WATER
AIR-SEA MEASUREMENT PLATFORM**

by

Vincent D. Chamberlain III

December 2020

Thesis Advisor:
Co-Advisor:

James H. MacMahan
Edward B. Thornton

Approved for public release. Distribution is unlimited.

THIS PAGE INTENTIONALLY LEFT BLANK

REPORT DOCUMENTATION PAGE			<i>Form Approved OMB No. 0704-0188</i>	
Public reporting burden for this collection of information is estimated to average 1 hour per response, including the time for reviewing instruction, searching existing data sources, gathering and maintaining the data needed, and completing and reviewing the collection of information. Send comments regarding this burden estimate or any other aspect of this collection of information, including suggestions for reducing this burden, to Washington headquarters Services, Directorate for Information Operations and Reports, 1215 Jefferson Davis Highway, Suite 1204, Arlington, VA 22202-4302, and to the Office of Management and Budget, Paperwork Reduction Project (0704-0188) Washington, DC, 20503.				
1. AGENCY USE ONLY (Leave blank)		2. REPORT DATE December 2020		3. REPORT TYPE AND DATES COVERED Master's thesis
4. TITLE AND SUBTITLE I-SPAR BUOY: DESIGN OF A LIGHTWEIGHT SHALLOW WATER AIR-SEA MEASUREMENT PLATFORM				5. FUNDING NUMBERS
6. AUTHOR(S) Vincent D. Chamberlain III				
7. PERFORMING ORGANIZATION NAME(S) AND ADDRESS(ES) Naval Postgraduate School Monterey, CA 93943-5000				8. PERFORMING ORGANIZATION REPORT NUMBER
9. SPONSORING / MONITORING AGENCY NAME(S) AND ADDRESS(ES) N/A				10. SPONSORING / MONITORING AGENCY REPORT NUMBER
11. SUPPLEMENTARY NOTES The views expressed in this thesis are those of the author and do not reflect the official policy or position of the Department of Defense or the U.S. Government.				
12a. DISTRIBUTION / AVAILABILITY STATEMENT Approved for public release. Distribution is unlimited.				12b. DISTRIBUTION CODE A
13. ABSTRACT (maximum 200 words) An Inner-shelf SPAR buoy (I-SPAR) for measuring atmospheric fluxes was developed for use in 7–20 m water depth as part of the ONR Coastal Land Air Sea Interaction (CLASI) effort. The design requirements are: 1) measurements obtained above the wave boundary layer (>4 m above sea level), 2) lightweight (< 100 kg), 3) dynamically stable, 4) modular for small boat transportation and deployment, and 5) able to acquire data for two months. The designed I-SPAR buoy has a 9 and 11 m length based on water depth and weighs 92 kg. The I-SPAR has an in-line configuration to reduce asymmetric wind drag. Atmospheric fluxes are estimated using a standard eddy-covariance, moving-platform technique that requires a fast-sampling sonic anemometer and inertial motion unit (IMU) to remove buoy motions and provide measurements in a geographic coordinate frame. The technique is modified by using a data-fused, Kalman filter IMU output. The I-SPAR is built with lightweight, high-strength carbon fiber tubes that are interconnected. The I-SPAR will follow low-frequency swell, where high-frequency wind waves are filtered out with a bottom damping plate. It is also designed for a maximum static tilt of 25° and a dynamic roll of 5.6° when exposed to a 15 m/s wind using vertical fins. A collocated solar-powered battery float will provide continuous power at a 50% duty cycle and includes an iridium modem for transmitting bulk statistics, including fluxes as well as providing a safety watch circle.				
14. SUBJECT TERMS air-sea interaction, atmospheric fluxes, CLASI, eddy-covariance, I-SPAR, inner-shelf, Kalman filter, momentum flux, shallow water, SPAR buoy, temperature flux, wind stress				15. NUMBER OF PAGES 85
				16. PRICE CODE
17. SECURITY CLASSIFICATION OF REPORT Unclassified		18. SECURITY CLASSIFICATION OF THIS PAGE Unclassified		19. SECURITY CLASSIFICATION OF ABSTRACT Unclassified
20. LIMITATION OF ABSTRACT UU				

THIS PAGE INTENTIONALLY LEFT BLANK

Approved for public release. Distribution is unlimited.

**I-SPAR BUOY: DESIGN OF A LIGHTWEIGHT SHALLOW WATER AIR-SEA
MEASUREMENT PLATFORM**

Vincent D. Chamberlain III
Lieutenant Commander, United States Navy
BA, Thomas A Edison State College, 2010

Submitted in partial fulfillment of the
requirements for the degree of

**MASTER OF SCIENCE IN METEOROLOGY AND PHYSICAL
OCEANOGRAPHY**

from the

**NAVAL POSTGRADUATE SCHOOL
December 2020**

Approved by: James H. MacMahan
Advisor

Edward B. Thornton
Co-Advisor

Peter C. Chu
Chair, Department of Oceanography

THIS PAGE INTENTIONALLY LEFT BLANK

ABSTRACT

An Inner-shelf SPAR buoy (I-SPAR) for measuring atmospheric fluxes was developed for use in 7–20 m water depth as part of the ONR Coastal Land Air Sea Interaction (CLASI) effort. The design requirements are: 1) measurements obtained above the wave boundary layer (>4 m above sea level), 2) lightweight (< 100 kg), 3) dynamically stable, 4) modular for small boat transportation and deployment, and 5) able to acquire data for two months. The designed I-SPAR buoy has a 9 and 11 m length based on water depth and weighs 92 kg. The I-SPAR has an in-line configuration to reduce asymmetric wind drag. Atmospheric fluxes are estimated using a standard eddy-covariance, moving-platform technique that requires a fast-sampling sonic anemometer and inertial motion unit (IMU) to remove buoy motions and provide measurements in a geographic coordinate frame. The technique is modified by using a data-fused, Kalman filter IMU output. The I-SPAR is built with lightweight, high-strength carbon fiber tubes that are interconnected. The I-SPAR will follow low-frequency swell, where high-frequency wind waves are filtered out with a bottom damping plate. It is also designed for a maximum static tilt of 25° and a dynamic roll of 5.6° when exposed to a 15 m/s wind using vertical fins. A collocated solar-powered battery float will provide continuous power at a 50% duty cycle and includes an iridium modem for transmitting bulk statistics, including fluxes as well as providing a safety watch circle.

THIS PAGE INTENTIONALLY LEFT BLANK

TABLE OF CONTENTS

I.	INTRODUCTION.....	1
II.	I-SPAR DEVELOPMENT AND DESIGN	5
A.	I-SPAR MODULES	6
1.	Electronics Module	8
2.	Spar Module	12
3.	Ballast/Damping Module.....	13
4.	Power Module.....	14
5.	Mooring Module.....	15
B.	I-SPAR COST	15
C.	PROTOTYPE DEVELOPMENT	16
D.	DEPLOYMENT DESIGN.....	17
III.	PLATFORM MOTION CORRECTIONS TO ENU	21
IV.	DYNAMIC STABILITY DESIGN AND MODELING	31
A.	DESIGN PHILOSOPHY.....	31
B.	STATIC TILT AND OPTIMAL ATTACHMENT POINT.....	31
C.	SPECTRAL WAVE FORCING.....	33
D.	HEAVE DYNAMICS OF BUOY	35
E.	ROLL DYNAMICS OF BUOY	39
V.	DISCUSSION	45
A.	STATIC TILT	45
B.	HEAVE DYNAMICS	46
C.	ROLL DYNAMICS	47
VI.	SUMMARY	49
	APPENDIX A	53
	APPENDIX B	55
	APPENDIX C	57
	LIST OF REFERENCES.....	59
	INITIAL DISTRIBUTION LIST	65

THIS PAGE INTENTIONALLY LEFT BLANK

LIST OF FIGURES

Figure 1.	Drawing of version 2 of the I-SPAR buoy.....	7
Figure 2.	The I-SPAR electronics module.	9
Figure 3.	Drawing for the I-SPAR buoy ballast assembly.	13
Figure 4.	A picture of the prototype I-SPAR and its mooring float deployed off Del Monte Beach, Monterey Bay, California.	17
Figure 5.	Cartoon depiction of the intended deployment of the I-SPAR system.	19
Figure 6.	Schematic of the coordinate systems used in a) Edson et al. (1998), b) the IMU, and c) the anemometer.	21
Figure 7.	Schematic of the Euler angle rotations about each axis.....	23
Figure 8.	Spectra for pitch and roll from an ocean prototype I-SPAR deployment on 10 January 2020 in Monterey Bay, CA.....	24
Figure 9.	Schematic of wind and ocean current profiles.....	32
Figure 10.	Tilt of the buoy due to wind forces and ocean current forces with moments about CG.	33
Figure 11.	Schematic of buoy with variables defined for heave dynamics.....	36
Figure 12.	Heave transfer function based on damping plate radius.	39
Figure 13.	Buoy rotation due to wave forcing and damping motions.....	40
Figure 14.	Plot of the distribution of the various moments in the roll dynamic equation over the vertical.....	43
Figure 15.	Plot of the variation of the various moments in the roll dynamic equation as a function of frequency.	44
Figure 16.	Plot of the heave response to wave interaction.	47
Figure 17.	Plot of the roll response to wave interaction.....	48

THIS PAGE INTENTIONALLY LEFT BLANK

LIST OF TABLES

Table 1.	Summary of results for $W_{10} = 15 \text{ ms}^{-1}$, $U=0$, $H_{\text{sig}}=5.5 \text{ m}$, $H_{\text{rms}} \approx H_{\text{heave}} \approx 4 \text{ m}$	45
Table 2.	I-SPAR components for 11 m with weight and distance from MSL.	57

THIS PAGE INTENTIONALLY LEFT BLANK

LIST OF ACRONYMS AND ABBREVIATIONS

A	Cross Sectional Area
A_B	Area of Buoyancy
A_D	Area of Damping Plate
A_{ENU}	Acceleration in East, North, Up
$A[f]$	Acceleration in Frequency Domain
$A(f)$	Wave Amplitude
Ah	Ampere Hour
AHRS	Altitude Heading and References System
A_{OBS}	Acceleration Observations
ASIS	Air Sea Interaction Spar
a [t]	Accelerometer Time Signal
B	Velocity Damping Parameter
b_0, b_1, b_2	B Coefficients for Linear Regression
C	Buoyancy Damping
C_d	Drag Coefficient in Water
C_{da}	Drag Coefficient in Air
CG	Center of Gravity
cm	Centimeter
c_p	Wave Phase Speed
D	Wave Drag
df or Δf	Sample Rate in Frequency
DFT	Discrete Fourier Transform
dt	Sampling Rate in Time
EKF	Extended Kalman Filter
ENU	East, North, and Up
FFT	Fast Fourier Transform
f_{nh}	Natural Frequency of Oscillation in Heave

f_{nr}	Natural Frequency of Oscillation in Roll
F_C	Current Force
F_D	Drag Forcing
F_I	Inertial Forcing
F_P	Pressure Forcing
F_η	Sea Surface Forcing
F_W	Wind Force
GB	Distance from Center of Buoyancy and the CG
GPS	Global Positioning System
h	Water Depth
$H[f]$	Frequency Response Function
H_{heave}	Heave Transfer Function
hp	High Pass Filtered
$H_p(z)$	Wave Velocity Transfer Function – Pressure
H_{rms}	Root-Mean-Square Wave Height
H_{roll}	Roll Transfer Function
HSI	Hard/Soft Iron
$H_u(z)$	Wave Velocity Transfer Function – Horizontal
$H_w(z)$	Wave Velocity Transfer Function – Vertical
I	Inertia
I-SPAR	Inner-Shelf SPAR
IFFT	Inverse Fast Fourier Transform
IMU	Inertial Measurement Unit
k	Wave Number
K	Kelvin
kg	Kilogram
k_s	Spring Coefficient
L_D	Depth of Damping Plate
L_s	Height of Top of Buoy

m	Meter
m_a	Mass
M_D	Velocity Wave Forcing Moment
MEMS	Micro-electromechanical System
mg	Milli G
M_I	Inertial Wave Forcing Moment
M_R	Wave Slope Disturbing Moment
ms⁻¹	Meter per Second
MSL	Mean Sea Level
N	Record Length
P	Transformation Matrix – Tilt
P	Pressure Force on Buoyancy
Q	Wave Inertia
rh	Relative Humidity
R	Position Vector of IMU
RMS	Root-Mean-Square
S_{roll}	Roll Spectrum
stds	Standard Deviation
SWH	Significant Wave Height
S_Y(f)	Heave Spectrum
S_η(f)	Surface Wave Spectrum
T	Transformation Matrix
t	Time
u	Horizontal Wind (east/west component)
U	Water Current
U₁₀	Wind Speed at 10 m
v	Horizontal Wind (north/south component)
V_{dc}	Volts Direct Current
V_{ENU}	Wind Vector in East, North, Up

$\mathbf{V}_{E'N'U'}$	Wind Vector in East, North, Up (before tilt removal)
$\mathbf{V}[f]$	Velocity in Frequency Domain
\mathbf{V}_N	VectorNav
$\mathbf{V}[t]$	Velocity in Time Domain
w	Vertical Wind
WBL	Wave Boundary Layer
\mathbf{X}	Cross Product
z	Height
Σ	Summation Operator
η	Sea Surface Elevation
$\boldsymbol{\Omega}$	Rotational Velocity Vector
$\boldsymbol{\Omega}_{\text{OBS}}$	Rotational Velocity Observations
ω	Angular Frequency
φ	Phase Spectrum
ϕ	Roll
ψ	Yaw
θ	Pitch
θ_{tilt}	Angle of Static Tilt

ACKNOWLEDGMENTS

Jamie, thank you so much for being my advisor and helping me get to the end! Your excitement to learn and teach is infectious, which made the process more enjoyable. Thank you for building a team concept with all your students and including each one of us in other projects. I will miss the field experiments and our lunch discussions.

Ed, thank you for being my co-advisor and teaching me everything you know about buoy dynamics and coding. I enjoyed our talks over Teams, just wish we would have had more time in person.

Paul, Keith, and Tim, thank you for allowing me to be involved in the behind-the-scenes work and teaching me about your experiences with electronics, small boat operations and field experiments. You made my thesis process fun, and I always looked forward to our interactions.

METOC professors and staff, thank you for making our time here a rewarding experience. You each had your own approach, but the linking factor was your passion for teaching.

Amanda, Bill, Jason, Josh, Justin, Ty . . . Greatest Cohort Ever. I can't say enough how amazing you all made this experience. Regardless of good days or bad, we were always there for each other. I can't wait to see the countless successes of our group!

Wendy, Joseph, and Brianna, thank you all for your unwavering support throughout graduate school and my thesis. I know things were challenging at times, but your love and encouragement always kept me going!

THIS PAGE INTENTIONALLY LEFT BLANK

I. INTRODUCTION

Over the last decade, observations of wind stress along the inner shelf were found to be larger than open-ocean formulations (Ortiz-Suslow et al. 2015; Shabani et al. 2016; Chen et al. 2018). In the open-ocean, it is well-documented that sea and swell waves modify the momentum flux (wind stress) (Donelan et al. 1997, amongst many others). Whether the waves positively or negatively contribute to the wind stress depends on the relative wave phase speed (c_p) to wind speed (U_{10}) ratio (defined as $c_p/U_{10} > 1.14$ for swell conditions, Höglström et al. 2015). When the waves are faster (slower) than the wind, the flux is upward (downward) (Donelan et al. 1997; Grachev and Fairall 2001; Kahma et al. 2016). The inner shelf primarily represents the region of wave shoaling. Zhao et al. (2015) and Chen et al. (2018) showed that wind stress differences are related to the shoaling surface gravity waves. The wave phase speed decreases, and the wave height increases due to shoaling waves into shallower water depths. Ortiz-Suslow et al. (2018) compared some small boat observational case studies along the inner shelf to empirically-derived formulations by Höglström et al. (2015). Chen et al. (2018) has explicitly stated the importance of shoaling waves and their influence on wind stress using theoretical formulations by Semedo et al. (2009). In the open ocean, the angle of the wind stress is dependent on the direction of the wind compared to the swell waves (Geernaert et al. 1993; Rieder et al. 1994; Grachev et al. 2003) as well as the direction of strong surface currents that will influence the waves (Zhang et al. 2009). Similarly, Chen et al. (2018) found for the inner shelf that the stress angle can vary significantly under low wind and swell wave conditions. The inner shelf is unique as it supports diurnal, thermally-driven sea breeze and land breezes that modify ocean waves, surface currents, and mixing (Villas Bôas et al., 2019). Though fundamental progress has been made for air-sea interactions along the inner shelf, more field observations are required at multiple field locations at differing depths for long durations (e.g., month) to fully address the impact of shoaling waves on wind stress.

For the inner shelf, measurement platforms that extend several meters above the sea surface can be either fixed or floating. There are limited fixed platforms (Mahrt et al. 1996; Chen et al. 2018, 2019), owing to the structures that can annually withstand high

winds, large waves, salt-water corrosion, and piling scour, as well as the resources for structure maintenance. Piers can be a useful fixed structure (Grachev et al. 2017); however, their size can negatively influence observations and thus limit conditions for unobstructed wind measurements, which can unintentionally bias interpretation for winds from certain directions (Grachev et al. 2017). An alternative to fixed structures are short-term (several months) floating platforms. These provide flexibility in deployment regions and locations, and are generally smaller in size reducing platform interference in the wind observations, and have been successfully used throughout many large-scale experiments (Drennan et al. 1996; Edson et al. 2013; Bourras et al. 2019). Floating platforms include various shaped moored and drifting buoys that range from wide discus platforms to more slender spar buoys (Ancil et al. 1994; Graber et al. 2000; Weller et al. 2012; Drennan et al. 2014; Flüggé et al. 2019). Each buoy design has positives and negatives. The wide platforms incur less tilt but are excited by high frequency waves and disturb the surrounding water (Graber et al. 2000). The slender spar buoys tend to follow the low frequency waves and tend not to disturb the water, but will incur more tilt in high winds unless mitigated by design. Additional types of platforms that have been outfitted include small research vessels (Ortiz-Suslow et al. 2015, 2018), unmanned surface vehicles like the Ocarina, a wave following trimaran (Bourras et al. 2014), a wind powered Saildrone (Zhang et al. 2019), and FLIP (Fisher and Spiess, 1963), which have made significant contributions to air sea fluxes (Rieder et al. 1994; Grachev et al. 2003; Miller et al. 2008), but are not the focus herein.

For many moored floating platforms, wind turbulences are generally obtained with a fast-sampling (i.e. 20 Hz) sonic anemometer, so that eddy-covariance methods can be applied for estimating momentum fluxes (Edson et al. 1998, amongst others). This approach requires synchronous, high-frequency measures of the platform through an inertial motion unit (referred to as IMU) so that platform motions can be removed as well as data transformed into a common coordinate frame, such as East, North, and Up (ENU) (Edson et al. 1998; Miller et al. 2008). Though platform motions can be measured with high fidelity, an initial design objective is to have the moored platform to be wave following (Graber et al. 2000), and to ensure that it remains fairly upright, and resonance

responses are mitigated (Edson et al. 1998, Graber et al. 2000). One of the most common floating platforms is the Air Sea Interaction Spar (ASIS) buoy, where the design combines the stability attributes provided by a SPAR buoy design used in R/P FLIP with the wave following characteristics of a lightweight discus buoy (Graber et al. 2000). The ASIS buoy weighs 1293 kg and is 11 m long (Graber et al. 2000). Owing to its weight a large ocean class research vessel is required for deployment that limits the deployable water depth to about 25 m (H. Graber, personal communication). ASIS buoys have been successfully deployed around the world and have been a fundamental asset for most large collaborative air-sea experiments, such as FETCH (Drennan et al. 2003), Shoaling Waves Experiment (Zhang et al., 2009), Southern Ocean Gas Exchange experiment (Sahlée et al., 2012), amongst others. Flügge et al. (2016) developed a smaller-ASIS like buoy and found good agreement with wind stresses at a nearby fixed ASI tower using the motion corrections by Edson et al. (1998).

The inner shelf presents new logistical challenges for obtaining observations using small vessels, particularly atmospheric. The primary difficulty is that for shallower water depths, the tidal amplitude as well as wave height increases in relative importance to the water depth. In general, the length and draft of the vessel is related to the water depth for allowable deployments deemed safe. Smaller vessels can safely operate in shallow-water depths of the inner shelf. However, these vessels become more limited in their ability to deploy moorings of certain shapes, lengths, and weight. Using small vessels as the measurement platform also tends to be more limited, as smaller vessels provide less shelter and are limited in at-sea comforts, so observations are reduced to short durations during daylight hours, as well as limited sea conditions. The small vessels that can operate in the inner shelf will impact the design of the measurement platform.

An Inner-shelf SPAR (I-SPAR) buoy has been developed for operations ranging from 7 m to 20 m water depth with a measurement height of 5 m above MSL. The I-SPAR will support single-element array of sensors at height of 5 m to allow the I-SPAR to be nearly symmetric and inline above and below the MSL (Chapter II). The single-element instruments include a sonic anemometer, Global Positioning System (GPS) aided IMU, temperature and humidity sensor, and data acquisition system (Chapter II). The I-SPAR

will be powered with a separate solar panel buoy that will also provide power to charge the batteries during daylight hours. This will provide sufficient power to calculate real-time bulk statistics (e.g., means, stds, and stresses) onboard and iridium communication with shore. A modified motion-correct procedure by Edison et al. (1998) is developed. The modifications incorporate new technological advances associated with the IMU and increased onboard computational improvements with the data acquisition system (Chapter III). The newest IMUs provide highly-accurate, real-time measures of pitch, roll, and yaw obtained through sensor fusion of accelerometer and gyroscope data (Sabatini, 2011), eliminating the need for selecting an arbitrary cut-off frequency for complementary filters as outlined in Flugge et al. (2016). Furthermore, Fourier transforms can be performed for integrating IMU accelerations eliminating phase shifts that occur with time-domain integrations (Brandt and Brincker, 2014). The I-SPAR mooring is designed to operate in winds up to 15 ms⁻¹ and waves up to 5.5 m. The model for the design parameters is described in Chapter IV.

II. I-SPAR DEVELOPMENT AND DESIGN

The Inner-shelf SPAR buoy (I-SPAR) is designed to operate from 20 m water depth to as shallow as possible while remaining outside of depth-limited breaking waves, referred to as the surf zone. There are a number of critical considerations for the I-SPAR, including the height of observations, size and weight of the buoy, dynamical response to winds and waves, as well as anticipated environmental conditions. The design also requires the incorporation of specific meteorological and motion sensors and a power module for long (e.g., 1–2 months) deployments.

Observations of wind turbulence need to be obtained at 5 m above the sea surface, which is suggested to be above the wave boundary layer (Chalikov and Rainchik, 2011; Edson et al. 2013), though others (e.g., Chen et al., 2019) have suggested that the wave boundary layer extends well above 5 m during light winds. One goal is to keep the subaqueous portion of the buoy as short as feasible to deploy in as shallow of water as possible. A reasonable initial assumption is that the subaqueous portion would be approximately 5 m, equal to that of the 5 m subaerial portion. With a 5 m subaqueous portion, a 2 m tidal range in Monterey Bay, CA, a 2 m root-mean-square wave height (H_{rms}), and a 1 m water depth safety factor, the shallowest the system can be deployed in is 8 m water depth in mean sea level, MSL (i.e., 7 m at low tide). Ignoring the length of the bottom section, a 2 m H_{rms} will break in approximately 4 m water depth (Thornton and Guza, 1983) at low tide, or 5 m water depth at MSL. The buoy needs to be deployed outside of wave breaking so adding 1 m water depth for safety suggests that the shallowest water depth to be seaward of wave breaking would be 5 m at low tide (6 m MSL). Therefore, 6 m MSL is the shallowest water depth based on solely on wave breaking, tidal range, and safety factor. This would require a 4 m subaqueous portion, which is evaluated in Chapter IV.

The buoy size and weight are a further limiting factor for small vessel deployment. Based on personal field experience deploying small moorings by hand, 36 kg was regarded as a safe upper limit for human lifting. As will be shown, the I-SPAR total weight had to be larger than 36 kg. This will require special, small boat rigging, which is not discussed

herein. The length of the buoy needs to be supported by the length of the vessel or be modular in design, such that shorter sections can be transported, and the buoy built in sections at sea at the location of deployment. All of these small vessel logistical elements resulted in a spar-like buoy form factor. The diameters of the SPAR elements are discussed in Section II.A.2.

Since the buoy is designed to be a spar-like buoy, another important aspect of the buoy design was to have it nearly symmetrical about the horizontal to ensure wind, wave or current forces do not rotate the buoy. This required the electronics and sensors to be placed inline over the vertical to minimize any windage elements that could result in preferential static tilt.

The I-SPAR is designed with an optimal goal of 100% duty cycle (sampling continuously) for 2 months. A minimum goal of 50% duty cycle (sampling every hour for 30 minutes) for 2 months. The instruments, data acquisition system (DAS), and power module will influence this design aspect.

Lastly, a goal is to deploy 10 I-SPARs to provide adequate spatial coverage during field experiments. The goal of 10 I-SPARs influenced the material and equipment cost of the I-SPAR, which generally focused on using as many commercial off-the-shelf components as possible, and limiting custom parts. For 10 I-SPARs to be deployed for 2 months, and to limit logistical costs of watching the I-SPARs, iridium communications were deemed critical for evaluating the various onboard sensors and monitoring the I-SPAR watch circle.

A. I-SPAR MODULES

The I-SPAR is organized into four major modules: the electronics module, spar module, ballast/damping module, and the power module (Figure 1). The electronics module is the uppermost section and includes the sensors and DAS required for direct covariance flux measurements (Figure 1a). The spar module is the middle structure of the buoy, which includes the carbon fiber tubes and buoyancy sphere (Figure 1b). The ballast/damping module is the lower section of the buoy, where the ballast is located to obtain a low center of gravity (CG) and includes the damping plate for vertical motions

and fins for horizontal motions (Figure 1c). The power module includes the solar powered rechargeable battery buoy and wiring components that connect into the electronics module (Figure 1d). Each component of the buoy is critically important as they have an integrated impact on the total design. The components were judiciously selected based on their capability and impacts on the total system.

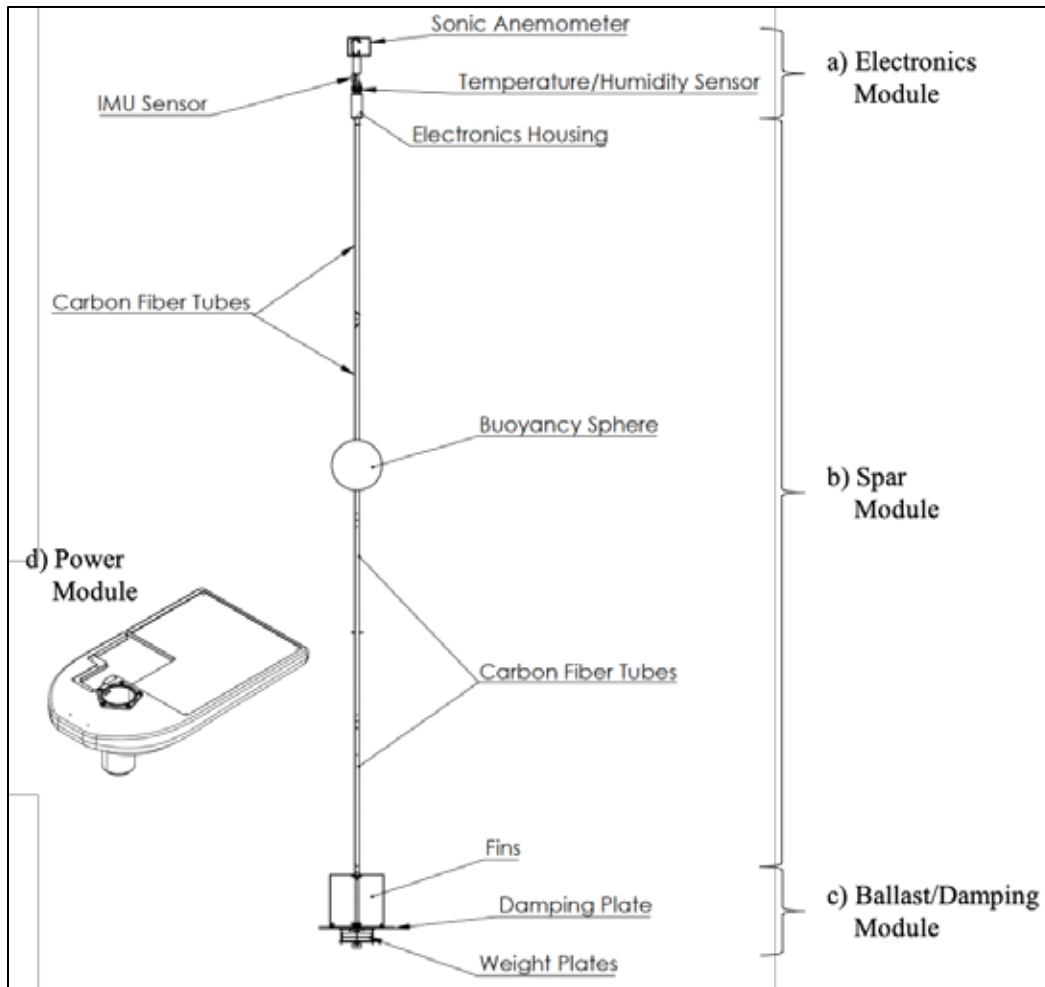


Figure 1. Drawing of version 2 of the I-SPAR buoy. The electronics assembly (a) is the uppermost section and contains all electronics components. The spar module (b) is the center section and contains the carbon fiber tubes and the buoyancy sphere. The ballast/damping module is at the bottom and contains the weight plates, damping plate, and fins. The power module (d) is adjacent to the I-SPAR and connected with a smart mooring line.

1. Electronics Module

The wind stress and sensible heat flux will be estimated at 5 m elevation using the eddy-covariance technique (Oost et al. 1993; Smith et al., 1995, Edson et al. 1998), which requires high frequency measurements of wind velocities and temperature typically obtained by an ultrasonic anemometer. The R.M. Young (model 81000, Figure 2a) was chosen as the best cost-effective ultrasonic anemometer for measuring the three-components of wind velocities and sonic temperature. Mauder and Zeeman (2018) evaluated 7 different cost-effective ultrasonic anemometers and the R.M. Young model 81000 performed as well or better, respectively. The R.M. Young is known to more accurately measure sonic temperature and suggested as a reasonable model for this application (C. Fairall, personal communication). The system uses three pairs of opposing transducers to measure the wind flow with a 0.01 ms^{-1} resolution and a $\pm 1\%$ accuracy (R.M. Young Company 2006). The wind direction is measured in degrees with a 0.1° resolution and an accuracy of $\pm 2^\circ$ (R.M. Young Company 2006). The sonic temperature measurements have a $\pm 2^\circ\text{C}$ accuracy (R.M. Young Company 2006). An external (small) junction box is affixed to base of the anemometers base (Figure 2c). This represents the only non-symmetrical part of the I-SPAR, for which its size is considered minimal. Winds are described in the “from” direction, such that +v is a northerly wind (south-oriented vector), +u is an easterly wind (west-oriented vector), and +w is an upward wind coming from below. This frame of reference is important when describing the coordinate rotation (Chapter III). The sonic anemometer is located at the top of the I-SPAR (Figure 1a).

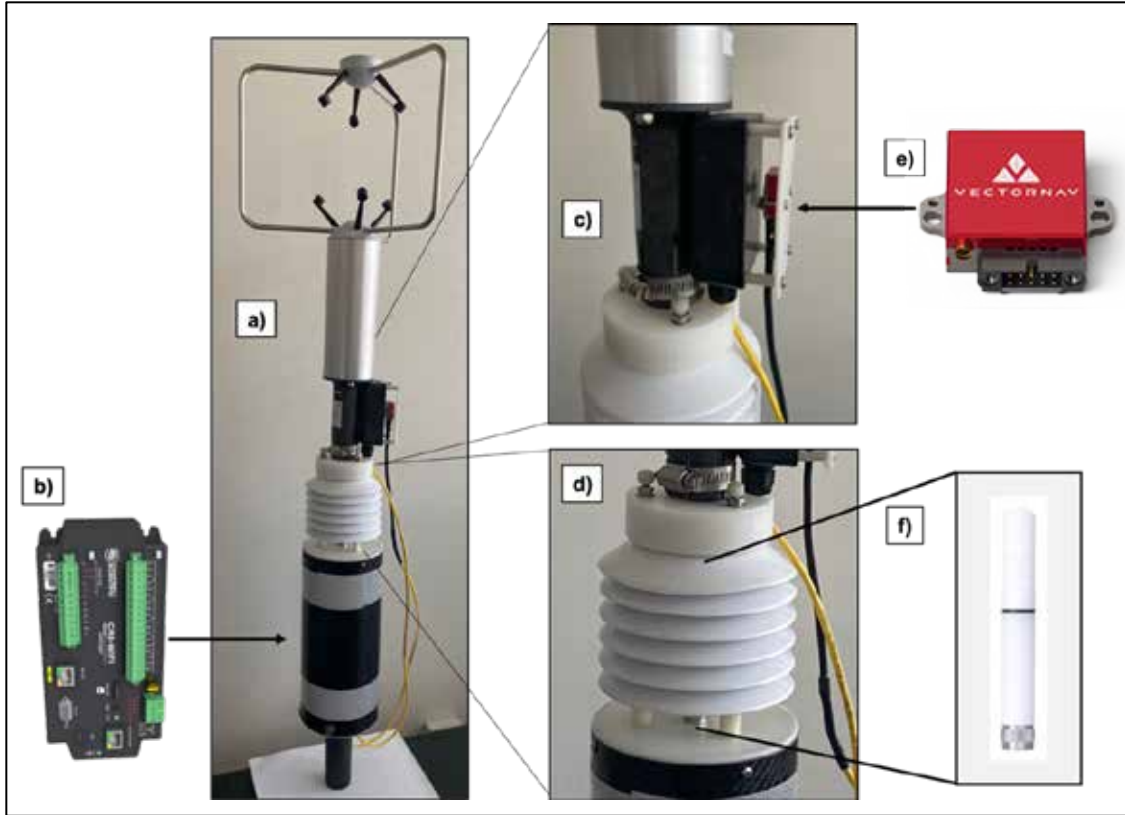


Figure 2. The I-SPAR electronics module. (a) contains the R.M. Young anemometer, VectorNav IMU, Rotronics T/H sensor, and the custom carbon fiber housing with the CR-6 DAS (b) mounted inside. The IMU (e) is mounted on the anemometer junction box (c). The T/H sensor (f) is threaded into the Delrin cap of the housing and covered by 6 radiation shields (d). Source: b) Campbell Scientific (2019); e) VectorNav Technologies (2020); f) Rotronic AD (2019).

A micro-electromechanical system (MEMS) Inertial Motion Unit (IMU) is required to measure the I-SPAR movements in order to remove these motions before the eddy covariance analysis is performed (Edson et al. 1998 and Miller et al. 2008). MEMS IMUs have significantly improved in performance over the past decade while reducing in size and cost from expensive macro sensors for large vehicles to micro sensors for smart phones (Shaeffer 2013). This growth can be attributed to the popularity of inertial sensor technology, for example, unmanned systems, robotics, virtual reality, and personal electronics devices for tracking tilt, positioning, and alignment (Brigante et al. 2011; Łuczak et al. 2017). There are a number of MEMS IMUs with a 3-axis gyroscope,

accelerometer, magnetometer, and GPS that provide real-time, low-latency estimates of pitch, roll, and yaw. Pitch, roll, and yaw are derived from sensor-fusion techniques (Sabatini, 2011, discussed in greater detail in Chapter III). The VectorNav (VN) 100 and 200 were chosen based on their onboard extended Kalman filter (EKF), capable of fusing data from the MEMS sensors to estimate the Euler angles of the platform. They contain an Altitude Heading and References System (AHRS) that is continuous over 360° (VectorNav Technologies 2020). The dynamic pitch/roll of the VN-100 is accurate to within 1.0° RMS; however, fusing GPS sensor data from the VN-200 improves the dynamic pitch/roll accuracy of the VN-200 to 0.03° (VectorNav Technologies, 2020). The gyroscope provides angular velocity measurements with an in-run bias stability of a maximum of 10°/hr (VectorNav Technologies 2020). The accelerometer provides accelerations with an in-run bias stability of <0.04 mg (VectorNav Technologies 2020). The GPS has a position accuracy of 1 m in the horizontal and 1.5 m in the vertical (VectorNav Technologies, 2020).

The IMU was placed in a vertical orientation and attached to the anemometer junction box (Figure 2c), which provide a relative short (35cm) distance to the anemometer's measurement location. The GPS antenna is a compact disk which is secured to the top of the anemometer as it needs a flat surface with an unobstructed view of the sky. Its cable is tightly fastened down to the anemometer support bar to connect to the IMU in order to prevent any corruption to the wind measurements by introducing artificial turbulence (Oost et al., 1993). The support bar for fastening will be on the opposite side of the mooring attaching point, which should be downwind. The axes of the IMU are transformed to reflect this orientation, where +X is away from the faceplate, +Y is to the starboard, and +Z is from the bottom of the IMU. Appendix A lists the system changes for the IMU in this configuration.

A temperature and humidity (T/H) sensor is required to describe the air properties, that are used to estimate sensible and latent heat fluxes (Edson et al. 1998; Cronin et al. 2019). A Rotronic Standard Meteo Probe model HC2A-S3 (Figure 2f) is one of the most compact transducers that has a temperature sensor accuracy of $\pm 0.1^\circ \text{ K}$ at 23° C with a range of -40 to $+60^\circ \text{ C}$ and a humidity sensor accuracy of $\pm 0.8\% \text{ rh}$ with a range of 0 to

100% rh (Rotronic AD 2019). With some slight modification, this model has the unique ability to be directly threaded into a custom housing using its weather-proof gasket.

The Rotronic T/H sensor was affixed to the top of the custom data acquisition housing (Figure 2d). This provided a few benefits. First by direct connection to the housing, it negated the need for an external power/data cable. It also allowed the sensor to be placed directly in the center maintaining the goal of inline and symmetry. Lastly, the six baffles (Figure 2d) that serve as a radiation shield to prevent direct sunlight provide the needed supporting structure for the sonic anemometer mounted above without adding any load or disturbing the T/H sensor.

The Campbell Scientific CR-6 DAS (Figure 2b) was chosen for synchronizing the data streams, storing the data, and performing onboard wind stress and sensible heat flux calculations. The CR-6 is a commonly used DAS in the meteorological community. There are a number of supporting aspects to the CR-6, such as online tutorials, existing online programs and examples, available technical support, and a number of colleagues that use the CR-6. The CR-6 allows for a plethora of data inputs. The onboard processor has enough memory and computational power to perform sophisticated data techniques, such as Fast Fourier Transforms. Fourier Transforms are important for integrating IMU accelerations to velocities without phase-shifting errors (Brandt and Brincker 2014). The data are stored on a removable 16GB microSD flash memory card allowing for long (e.g., 2 months) field collections. The CR-6 is available with different wireless communication options. For operations here, the CR-6 with the 2.4GHz wireless option allows users to evaluate logging and sensor status when in close proximity to the buoy. The wireless option required that the CR-6 be located above the sea surface. The DAS is housed in a protective, water resistant, 12.7 x 27.9 cm custom carbon fiber cylinder. It is hard sealed at the top with a 1.27 cm thick Delrin plastic cap. The bottom has a 2.54 cm thick Delrin plastic cap secured with bolts that provides access to the DAS and internal wiring. Two cable connectors were installed in the bottom Delrin cap to connect the anemometer and IMU power/data cables to the DAS.

The electronics module accounts for the top 97 cm of the buoy and weighs 3.78 kg. Ideally the weight should be as small as possible. All of the primary electronics (excluding

the battery) comprised one module that can be assembled on land before deployment (Figure 2a). The electronics module can be attached and removed easily from top of the I-SPAR.

2. Spar Module

There are three design considerations for the spar module of the platform. First, the body of the buoy must be lightweight with a goal of focusing most of the weight at the bottom. Second, it must be narrow in diameter to minimize wave, current and wind forces. Third it must be strong enough to withstand the dynamic loads of deploying and recovering. The buoy is designed using commonly available 5.08 cm (i.e. 2 inch) diameter carbon fiber tubes. Compared with aluminum, it has almost 4 times the tensile strength with 70% less density and does not corrode (Baskutis et al. 2014). Carbon fiber costs about 130% more than aluminum pipe, and the additional costs were deemed acceptable for a robust spar structure that can be deployed for 2 months in the ocean.

The modular design of the I-SPAR provides versatility for shipping and transporting the system on a small vessel. The spar module includes 5 carbon fiber tubes that are inter-connected using 30.5 cm carbon fiber inserts at the junctions. The subaerial portions of the buoy use a quick connect locking pin to quickly add or remove sections while working on the water. The subaqueous portion uses stainless steel bolts as oppose to locking pins to avoid inadvertent disconnection during deployment, potential line entanglement, or from drifting kelp.

The buoyancy element slides over the 5.08 cm diameter tubes. The buoyancy force (wet weight) was calculated by determining the dry weight of the system minus the weight of the seawater displaced by multiplying the volume of the submerged portion of the buoy with the density of seawater. Stability analysis (Chapter IV) determined that the surface area volume of water displaced by the buoy at MSL should be relatively large for the buoy to follow the waves and reduce the dynamic roll. A large (0.61 m) diameter Jim Buoy off-the-shelf flotation sphere is used as the buoyancy element. The buoyancy sphere increased the dry weight of the buoy.

3. Ballast/Damping Module

The ballast/damping module (Figure 3) represents both the ballast and damping elements, and are collocated at the bottom to keep the center-of-gravity, CG, as low as possible for stability. Ballast weight in a spar design provides a restoring force for the system during dynamic roll (pitch) movement. It also provides resistance to static tilt in high wind events. The weight needs to be sufficient enough to keep the system upright and stable but light enough to meet deployment requirements discussed above. A goal for the I-SPAR is to be wave following (e.g., heaving with the long period swell waves). A Delrin damping plate with a 0.91 m diameter and 1.3 cm thickness is used to dampen vertical motion excited by the high frequency wind waves. The amount of dampening is a function of the diameter of the damping plate and scales with weight distributions (Section IV.D).

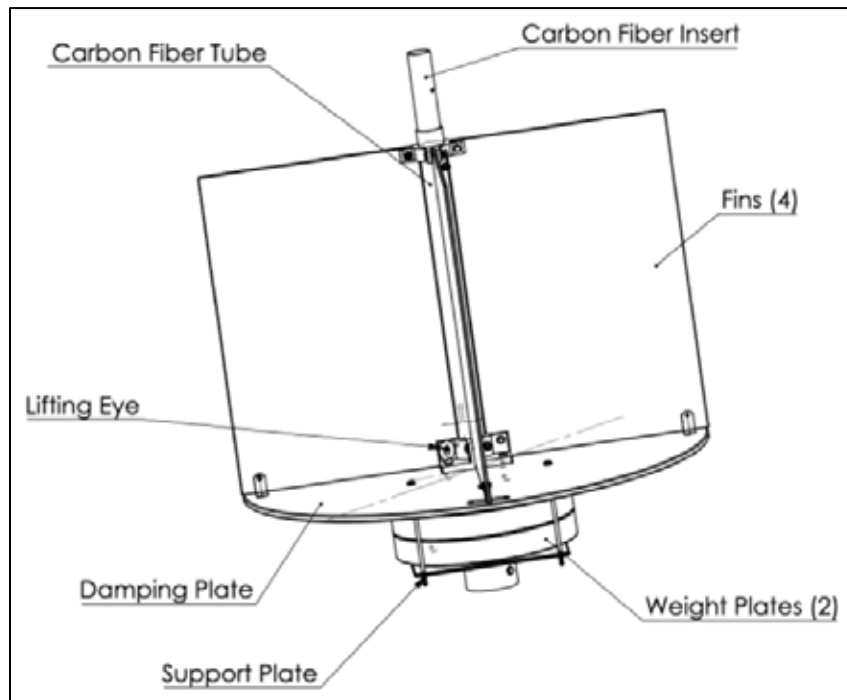


Figure 3. Drawing for the I-SPAR buoy ballast assembly. Four cross sectional fins are mounted to the damping plate and the carbon fiber insert. Beneath the damping plate are two weight plates used as the primary ballast. A carbon fiber tube insert extends through the center of the assembly with a support plate and bolted cap at the bottom.

Rotation about the vertical is damped using four rectangular fins. The fins are fabricated out of Delrin that are attached to the bottom damping plate and the carbon fiber insert. This improves the design in two ways. The force per unit area of ocean currents and wind are similar owing to the density differences of water and wind for wind driven currents. The increased subsurface area provided by the fins reduces the tilt of the buoy during higher winds.

The ballast is designed using a series of varying increment bar-bell weight plates that fit around 5.08 cm diameter pipe. This provides an easy and inexpensive option to adjust ballast. A lifting eye is mounted on the bottom assembly to aid in the deployment and recovery of the system. The bottom of the carbon fiber insert is left open to allow water to flood the bottom half of the carbon fiber tubes. This adds 10.25 kg of additional weight to the system when submerged which further increases stability.

4. Power Module

The power module is designed to supply power for near 100% duty cycle for a 2-month deployment. The anemometer requires a 12 Vdc input and draws 110 ma/hr. The T/H sensor requires a 3.3–5 Vdc input and draws 4.5 ma/hr. The IMU requires a 3.5–5.7 Vdc input and draws 40 ma/hr. The DAS has an input of 12–18 Vdc and has a power draw range of 67 ma/hr. This results in a total power draw of 222 ma/hr at 13.6 volts.

There were two alternatives for the power module. The first was to use existing underwater battery canisters commonly used for oceanographic equipment and their associated batteries. Based on the power requirements, this required lithium batteries, which are both costly and can be dangerous (Section II.C). After pilot deployment tests, it was believed that a more effective power module could be developed based on a surface float with a solar panel. This would provide continuous power well beyond two months and could be utilized for multiple deployments with reduced environmental waste. The initial cost is more, but minimal over multiple or longer deployments when considering longevity of the battery buoy (Section II.B).

Through a partnership with SOFAR Ocean, a solar rechargeable battery system, using the shell concept of their oceanographic spotter buoy (Raghukumar et al. 2019) was

developed. It uses a Sunpower 50 watt solar panel to provide unlimited endurance to the I-SPAR at 50% duty cycle, meaning that the system will turn on and record data for 30 minutes of every hour. The battery buoy is connected to the mooring float line with a rubber strain relief to decouple the movement of the battery system from the I-SPAR. A smart mooring line that contains the power cable runs from the mooring line to the I-SPAR and connects at the center of rotation. The connection point for the mooring float was lowered to the CG to decouple the motion of the power module and the mooring float from the motion of the I-SPAR. This is discussed further in Chapter IV. The power cable is carefully affixed to the spar module up to the electronics module, ensuring disturbance to the symmetric design is minimized.

5. Mooring Module

There are numerous options available for the mooring module (not pictured). The constraint was to keep the buoy on a relatively small watch circle to prevent grounding or interaction with the surf zone. A 0.46 m diameter Jim Buoy rope float is used to provide positive lift (Figure 4). The buoy is moored to the ocean floor with marine line connected to 15.9 kg of chain and a Manson anchor on the ocean floor.

B. I-SPAR COST

The I-SPAR buoy system costs \$23.2k per unit. The electronics module costs \$7.8k, which includes \$2.9k for the RM Young, \$3.0k for the VN-200, \$1.3 for the CR-6 with WIFI, and \$0.6k for the T/H sensor, baffles and housing material. The carbon fiber tubes (5) and connection inserts cost \$2.0k. For comparison, the aluminum pipes (5) would have cost \$1.5k but the benefit of carbon fiber was worth the additional cost. The flotation spheres for the buoyancy and the mooring costs \$0.7k. The ballast materials costs \$1k. The power buoy costs \$11.7k and includes the solar power buoy, iridium chip and access, and the service plan for real-time updates. The upfront cost of the battery buoy is estimated to be recouped in the first year of operation. For comparison during 3 planned experiments over the next year, it would have cost \$9.4k for six lithium-ion batteries (2 per deployment) and the storage canisters for each buoy that would provide two months of data for each experiment without the iridium or data page capability.

C. PROTOTYPE DEVELOPMENT

The I-SPAR prototype (Figure 4) was developed first and provided significant lessons learned. The prototype was 10 m long with 5 m above and below the surface, and weighed 40 kg. Custom high-density foam 18.42 cm diameter cylinders provided buoyancy. The bottom module consisted of an off-the-shelf Nortek pressurized battery canister, which housed the battery and additional lead shot for ballast. A 13.6-volt lithium-ion battery pack provided 171 Ah of power. Based on the power requirements, this would provide 51 days of power at an 80% efficiency. Directly above the battery housing was a 0.61 m diameter, 0.32 cm thick damping plate made of Delrin. With this configuration, the I-SPAR was modeled to have a dynamic roll of less than five degrees when exposed to a 20 ms^{-1} wind.

After preliminary deployment and float tests with the prototype, additional modifications were required. The battery canister and internal cable were removed due to the surface power module. This eliminated some of the complexity of attaching this module in the field on a small boat. By removing the battery canister from the bottom, it freed up more design options to improve the dynamics of the I-SPAR. These changes are incorporated in version 2 of the I-SPAR.

The power module, buoyancy element, damping plates and fins, length, and weight are changed for version 2 of the I-SPAR (Figure 1). The power module is a separate floating system. The buoyancy element changed from cylinders to a single sphere. The heave damping plate increased in diameter and vertical fins were added. Ballast changed from the battery canister, battery, and lead shot to barbell weights. The length of the system changed to lower the CG when operating in water greater than 9 m. The total weight of the I-SPAR increased to 81.4 kg.



Figure 4. A picture of the prototype I-SPAR and its mooring float deployed off Del Monte Beach, Monterey Bay, California. Taken on 10 January 2020, the image shows the 5 m subaerial portion of the buoy from the electronics module (Figure 2a) at the top to the flotation cylinders at MSL.

D. DEPLOYMENT DESIGN

The operational deployment concept for the I-SPAR system is depicted in Figure 5. The I-SPAR will be moored to a float that has an anchor line attached to 15.9 kg of chain and a Manson anchor on the ocean floor. The SOFAR battery buoy will be attached to the mooring line with a shock absorbing rubber line containing the power cable running to the

CG of the buoy and up to the electronics housing. A SOFAR spotter buoy will be deployed adjacent to the I-SPAR to measure ocean waves. The spotter buoy provides wind, wave, and sea surface temperature measurements in a trapezoidal shaped, lightweight, compact buoy (Raghukumar et al. 2019). The buoy is internally powered by a rechargeable lithium-ion battery that is augmented by solar panels on the top of the spotter. The buoy is designed to determine wave height to a 2 cm accuracy, wave period, and direction (Raghukumar et al. 2019). The winds are internally calculated by the spectral relationship between the winds and the waves (Raghukumar et al. 2019). Sea surface temperatures are measured by a digital thermometer mounted to its hull. An Acoustic Doppler Current Profiler will be deployed adjacent to the I-SPAR opposite of the SOFAR buoy. It uses five acoustic beams to provide a vertical profile of currents in the water column as well as the ability to calculate the Reynolds stresses in the ocean. The ADCP will be secured in a gimbaled tripod that will ensure a vertical orientation when deployed on the seafloor. The tripod will have a line extending to a 15.9 kg weight that is attached to a surface buoy to mark its position. There will be temperature sensors affixed to the vertical mooring line, positioned every one meter, to determine stratification of the water column.

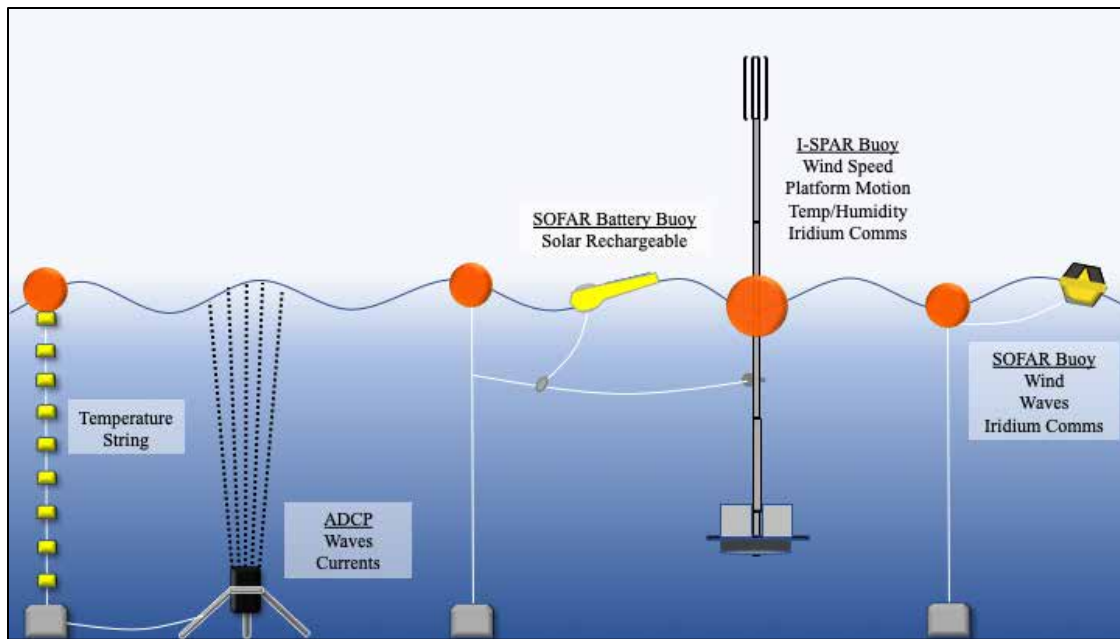


Figure 5. Cartoon depiction of the intended deployment of the I-SPAR system. The temperature string is attached to a mooring float that connects to the Acoustic Doppler Current Profiler tripod deployed adjacent to the I-SPAR. The I-SPAR buoy and battery buoy are attached to their mooring float. The SOFAR buoy and mooring float deployed adjacent to the I-SPAR.

THIS PAGE INTENTIONALLY LEFT BLANK

III. PLATFORM MOTION CORRECTIONS TO ENU

The data coordinate transformations into East, North, and Up (ENU) and buoy motion removal follows the procedures outlined in Edson et al. (1998), which has been successfully incorporated in many moving platform studies (McGillis et al. 2001; Hare et al. 2004; Weller et al. 2012; Blomquist et al. 2014). An illustration of the coordinate system by Edson et al. (1998) is provided in Figure 6a, where the I-SPAR IMU and the I-SPAR anemometer are provided in Figure 6b and c. The red vectors indicate vectors that should be aligned along the x-axis, green vectors should be aligned along the y-axis, and blue vectors should be aligned in the vertical direction. The vectors in the schematic are pointing towards the positive direction in its respective coordinate system. Appendix B lists the steps required to align the three coordinate systems.

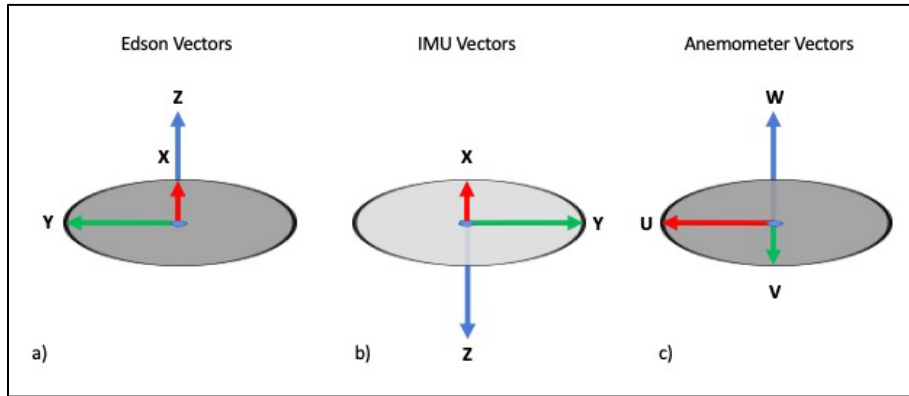


Figure 6. Schematic of the coordinate systems used in a) Edson et al. (1998), b) the IMU, and c) the anemometer. The red vectors represent vectors that should be aligned to the x-axis, green vectors should be aligned to the y-axis, and blue vectors should be aligned to the z-axis.

In a moving-reference frame, the wind vector (\mathbf{V}_{ENU}), where the subscript represents the reference frame and (E'N'U') represents the wind vector prior to tilt correction, is described by

$$\mathbf{V}_{E'N'U'} = \mathbf{T}(\mathbf{V}_{\text{OBS}} + \boldsymbol{\Omega}_{\text{OBS}} \times \mathbf{R}) + h_p \int \mathbf{T} \mathbf{A}_{\text{OBS}}, \quad (1)$$

$$\text{(Term 1)} \quad \text{(Term 2)} \quad \text{(Term 3)} \quad \text{(Term 4)}$$

where \mathbf{T} is the transformation matrix from the observed (OBS) platform frame to ENU, \mathbf{V}_{OBS} is the wind vector in the platform frame, $\boldsymbol{\Omega}$ is the rotational velocity vector of the buoy, \times denotes the vector cross product, \mathbf{R} is the position of the wind sensor with respect to the IMU, and \mathbf{A}_{OBS} is the observed accelerations of the buoy in the platform frame. The buoy rotation is defined by changes in the Euler angles, where yaw, ψ , is the rotation about the z-axis (Figure 7a), pitch, θ , is the rotation about the y-axis (Figure 7b), and roll, ϕ , is the rotation about the x-axis (Figure 7c). Positive rotations are clockwise for all axes. \mathbf{T} is defined as

$$\mathbf{T}(\phi, \theta, \psi)$$

$$= \mathbf{A}(\psi) \mathbf{A}(\theta) \mathbf{A}(\phi),$$

$$= \begin{bmatrix} \cos \psi & \sin \psi & 0 \\ -\sin \psi & \cos \psi & 0 \\ 0 & 0 & 1 \end{bmatrix} \begin{bmatrix} \cos \theta & 0 & \sin \theta \\ 0 & 1 & 0 \\ -\sin \theta & 0 & \cos \theta \end{bmatrix} \begin{bmatrix} 1 & 0 & 0 \\ 0 & \cos \phi & -\sin \phi \\ 0 & \sin \phi & \cos \phi \end{bmatrix},$$

$$= \begin{bmatrix} \cos \psi \cos \theta & \sin \psi \cos \phi + \cos \psi \sin \theta \sin \phi & -\sin \psi \sin \phi + \cos \psi \sin \theta \cos \phi \\ -\sin \psi \cos \theta & \cos \psi \cos \phi - \sin \psi \sin \theta \sin \phi & -\sin \theta \cos \phi \sin \psi - \sin \phi \cos \psi \\ -\sin \theta & \cos \theta \sin \phi & \cos \theta \cos \phi \end{bmatrix}, \quad (2)$$

where

$$\psi = \psi - 90^\circ. \quad (3)$$

90° must be subtracted from the yaw observations to align the mathematical coordinate system with the meteorological coordinate system for the coordinate transformation matrix to work correctly.

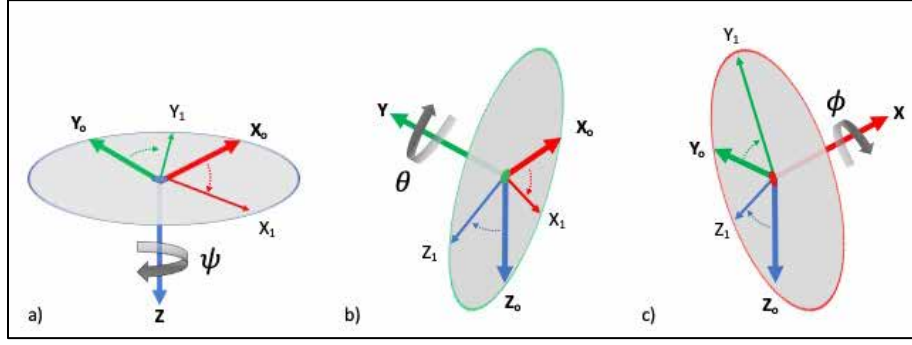


Figure 7. Schematic of the Euler angle rotations about each axis. a) yaw is about the z-axis, b) pitch about the y-axis, and c) roll about x-axis.

Pitch, roll, and yaw are estimated from the linear accelerations and angular velocities by the IMU. Flügge et al. (2016) and Edson et al. (1998) applied a complimentary filter to solve for the pitch and roll estimates by combining the low frequency contributions from the accelerations with the high frequency contributions from the angular velocities. The complimentary filter is designed to reduce the inherent errors in the low frequency drift of angular velocities and the high frequency noise in the accelerations. However, a cut-off frequency is required (Edson et al., 1998). There is uncertainty in selecting the appropriate cut-off frequency, which influences data results (Flügge et al., 2016). Herein, it is suggested to use the commonly-used EKF that are integrated into unmanned systems, virtual reality, and dynamic motion systems (Welch, 2009). The EKF have evolved to become a more accurate method for determining system orientations. It provides a blended solution for pitch, roll, and yaw across the transitional frequencies, where the complimentary filter frequency cut-off resides. The sensor fusion approach incorporates additional data fields (e.g., magnetic and GPS) that further reduce errors in pitch, roll, and yaw. During dynamic movements, the approach takes advantage of sensors that have high frequency accuracy with the reliability of the low frequency sensors to reduce drift errors, and vice-a-versa (Sabatini, 2011). Islam et al., (2017) found that the EKF is more precise and accurate compared to a complimentary filter and removes bias associated with selecting a frequency cut-off. The VectorNavs contains an onboard AHRS EKF algorithm that fuses data from the MEMS sensors and GPS, providing a real-time, high-frequency (up to 200Hz), accurate (yaw, pitch, and roll) output that can be applied to Equation 1.

For example, for the VectorNav 100 for the prototype buoy deployment, the internal AHRS pitch and roll are compared with the traditional estimates of pitch and roll estimated from accelerometer and gyroscope (Figure 8). The AHRS (blue line) solution matches the accelerometer observations (yellow line) at low frequencies and then the gyroscope observations (red line) at high frequencies. The AHRS pitch and roll are blended across the transitional frequencies. This avoids the need to select a complimentary filter frequency cut-off as described by Flügge et al. (2016). The use of the AHRS EKF is a deviation from the procedure by Edison et al. (1998).

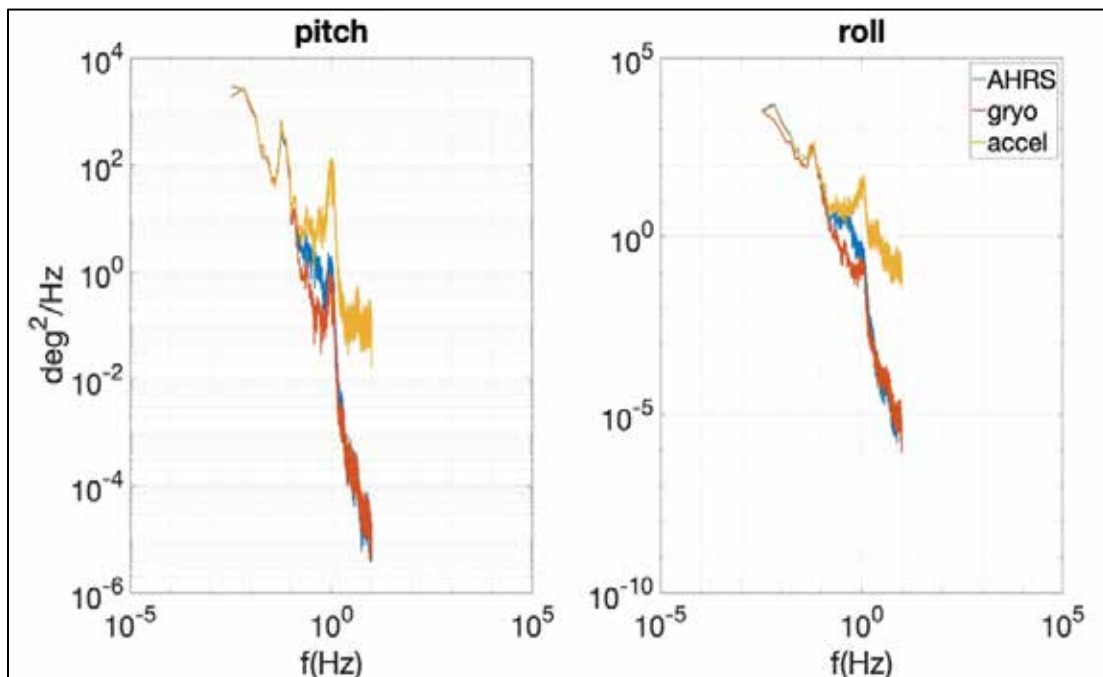


Figure 8. Spectra for pitch and roll from an ocean prototype I-SPAR deployment on 10 January 2020 in Monterey Bay, CA. Pitch (left) and roll (right) estimates spectra are described from AHRS (blue line), accelerations (yellow line), and rotational velocities (orange line).

Rotational velocities occur when the buoy rotates about one of its axes. This creates a translational velocity that also must be removed from the wind observations. Edison et al. (1998) introduced two methods for calculating the rotational velocity using observations from a gyroscope or the time rate of change of the Euler angles. Since we are using an IMU with a gyroscope output, this option was selected.

The IMU rotational velocities, Term 3 in Equation 1, about the three axes, denoted as $\mathbf{\Omega}$, in the platform frame of reference (subscript denoted by OBS). Since the IMU is attached to the I-SPAR, it is referred to as a strapped down system meaning that $\mathbf{\Omega}_{\text{OBS}}$ can be used to account for the angular velocities where

$$\mathbf{\Omega}_{\text{OBS}} = \begin{bmatrix} \Omega_{\text{OBS},X} \\ \Omega_{\text{OBS},Y} \\ \Omega_{\text{OBS},Z} \end{bmatrix}. \quad (4)$$

Since the IMU is not collocated with the sonic anemometer, the separation, \mathbf{R} , is included by

$$\mathbf{\Omega}_{\text{OBS}} \times \mathbf{R} = \begin{bmatrix} i & j & k \\ \Omega_{\text{OBS},X} & \Omega_{\text{OBS},Y} & \Omega_{\text{OBS},Z} \\ R_1 & R_2 & R_3 \end{bmatrix}, \quad (5)$$

and is expanded as

$$\begin{aligned} \Omega_X &= (\Omega_{\text{OBS},Y} * R_3 - \Omega_{\text{OBS},Z} * R_2)i \\ \Omega_Y &= -(\Omega_{\text{OBS},X} * R_3 - \Omega_{\text{OBS},Z} * R_1)j \\ \Omega_Z &= (\Omega_{\text{OBS},X} * R_2 - \Omega_{\text{OBS},Y} * R_1)k. \end{aligned} \quad (6)$$

The expanded form is required for the DAS as it does not support cross-product algorithm in its processing functions. Note expanded forms are provided throughout for the DAS programming. For the I-SPAR, the position of the IMU is fixed at $\mathbf{R} = [0.068, 0, 0.35]$.

The linear translational observations, Term 4 in Equation 1, are described next. Platform accelerations are rotated into ENU by

$$\mathbf{A}_{\text{ENU}} = \mathbf{T}\mathbf{A}_{\text{OBS}}, \quad (7)$$

and expanded as

$$\begin{aligned}
A_E &= T_{11} * A_{OBS,X} + T_{12} * A_{OBS,Y} + T_{13} * A_{OBS,Z} \\
A_N &= T_{21} * A_{OBS,X} + T_{22} * A_{OBS,Y} + T_{23} * A_{OBS,Z} \\
A_{UP} &= T_{31} * A_{OBS,X} + T_{32} * A_{OBS,Y} + T_{33} * A_{OBS,Z}.
\end{aligned} \tag{8}$$

The A_{ENU} are integrated to a frequency cut-off representing the high-pass filtered translational velocities defined as

$$V_{CM} = hp \int A_{ENU}. \tag{9}$$

Edson et al. (1998) stated that Term 2 in Equation 1 inherently removes the low-frequency translational velocities. The reasons for this currently elude the authors. The high-frequency portion still requires removal. The frequency cut-off is typically associated with the complimentary filter frequency cut-off, which is no longer used herein. The frequency cut-off for Equation 9 is determined by evaluating the ratio of the combined spectra of the pitch and roll computed solely from accelerations, compared to the combined spectra of the pitch and roll computed from the AHRS EKF method. The cut-off frequency for Equation 9 is determined when then ratio drops below 10, which is within one order of magnitude.

Brandt and Brincker (2014) demonstrated that integrations in the time-domain exacerbates inherent high frequency accelerometer drift with each time-step integration inducing phase shifts, unless a recursive filter is applied in the forward and backward time direction. They recommended integrations be performed in the frequency domain using discrete Fourier transform (DFT) with long time series. This resulted in small error rate and proved the most reliable method for signal integration. Here, a fast Fourier transform (FFT) is used to solve the DFT. Converting the time signal into the frequency domain using DFFT is given by

$$A[f] = \sum_{n=0}^{N-1} a[t] e^{-i\left(\frac{2\pi}{N}\right)fn}, \tag{10}$$

where $a[t]$ is the accelerometer time signal, N is the window size and equal to 2^p , f is the frequency index $(0,1,2,3,\dots,N-1)$ and equals $\left[\left(0:\frac{N}{2}\right),\left(-\frac{N}{2}+1:-1\right)\right] * df$, where $df = \frac{1}{N*dt}$, and n is the time index $(0,1,2,3,\dots,N-1)$, which is equal to the sampling rate (dt). The velocity spectrum ($V[f]$) is integrated by multiplying the $A[f]$ by the complex frequency response function, $H[f]$, so that

$$V[f] = A[f] * H[f], \quad (11)$$

where

$$H[f] = \frac{1}{\sqrt{-1} * 2\pi f}, \quad (12)$$

and for $f=1$ (zeroth frequency)

$$H[f] = 0.$$

$V(f)$ is high-pass filtered by the selected cut-off frequency and values are set to zero. $V(f)$ is converted to a time signal by an inverse fast Fourier transform (IFFT) given by

$$V[t] = \frac{1}{N} \sum_{f=0}^{N-1} V[f] e^{i\left(\frac{2\pi}{N}\right)fn}. \quad (13)$$

Term 4 in Equation 1 equals the real portion of $V[t]$.

A tilted or misaligned anemometer could skew flux measurements by as little as 10% but as much as 100% (Kaimal and Haugen, 1969). Edson et al. (1998) recognized that small tilts may still exist that bias the results associated with small errors in the electronics modules alignment. With the assumption that vertical velocity should equal zero over the open ocean a planar fit method outlined in Wilczak et al. (2001) is applied. The planar fit method uses multiple linear regression to define b coefficients (b_0, b_1, b_2) that can then be used to rotate the raw winds so that $\bar{w}=0$. To find the b coefficients, a pair of matrices is defined using the ENU winds,

$$\mathbf{X} = \begin{bmatrix} N & \sum e & \sum n \\ \sum e & \sum e^*e' & \sum e^*n' \\ \sum n & \sum n^*e' & \sum n^*n' \end{bmatrix} \text{ and } \mathbf{y} = \begin{bmatrix} \sum u^p \\ \sum u^*u^p' \\ \sum n^*u^p' \end{bmatrix}, \quad (14)$$

where N is the record length, Σ is the summation operator, and (') represents a deviation from the mean. The b coefficients can then be solved by using least squares matrix left division where

$$\mathbf{b} = \mathbf{X} \backslash \mathbf{y}. \quad (15)$$

Least squares matrix left division is available in most data analysis packages (e.g., Matlab) used on personal computers. For DAS, this was not available. Equation 15 is expanded to algorithms available on the DAS, as defined as

$$\mathbf{b} = (\mathbf{X}'\mathbf{X})^{-1}\mathbf{X}'\mathbf{y}. \quad (16)$$

The transformation matrix is defined as,

$$\mathbf{P} = \begin{bmatrix} \cos \theta & \cos \theta \sin \phi & \sin \theta \cos \phi \\ 0 & \cos \phi & -\sin \phi \\ -\sin \theta & \cos \theta \sin \phi & \cos \theta \cos \phi \end{bmatrix}, \quad (17)$$

where $\theta = \tan^{-1}(b_1)$ and $\phi = \tan^{-1}(-b_2)$.

The true winds computed in Equation 1 can be rotated to remove the anemometer tilt by the rotation matrix (\mathbf{P}),

$$\begin{bmatrix} V_E \\ V_N \\ V_{UP} \end{bmatrix} = \mathbf{P} \begin{bmatrix} V_{E'} \\ V_{N'} \\ V_{UP'} \end{bmatrix}, \quad (18)$$

where

$$V_{UP} = V_{UP'} - b_0. \quad (19)$$

Expanding the matrix multiplication yields

$$V_{\mathbf{E}} = P_{11} * V_{\mathbf{E}'} + P_{12} * V_{\mathbf{N}'} + P_{13} * V_{\mathbf{UP}'},$$

$$V_{\mathbf{N}} = P_{21} * V_{\mathbf{E}'} + P_{22} * V_{\mathbf{N}'} + P_{23} * V_{\mathbf{UP}'},$$

$$V_{\mathbf{UP}} = P_{31} * V_{\mathbf{E}'} + P_{32} * V_{\mathbf{N}'} + P_{33} * V_{\mathbf{UP}'}. \quad (20)$$

THIS PAGE INTENTIONALLY LEFT BLANK

IV. DYNAMIC STABILITY DESIGN AND MODELING

A. DESIGN PHILOSOPHY

The design goal was to keep the natural frequencies of oscillation as far away from the peak swell wave frequency as practical. Due to the light weight of the buoy, it is necessary to design a stiff system for heave natural frequency of oscillation. This means the buoy heave motion follows the wave and is in-phase with the waves.

The natural frequency of oscillation in heave was found by

$$f_{nh} = \frac{1}{2\pi} \sqrt{\frac{\rho g A}{m_a}} \approx 0.9 \text{Hz}, \quad (21)$$

where A is the cross-sectional area of the buoy at MSL and m_a is the mass of the buoy. The natural frequency of oscillation in roll was found by

$$f_{nr} = \frac{1}{2\pi} \sqrt{\frac{m_a g GB}{I}} \approx 0.4 \text{Hz}, \quad (22)$$

where GB is the distance between the center of buoyancy and the CG and I is the buoy inertia.

The design of the buoy is based first on the static tilt by the wind and then the dynamic heave and roll. The design condition is for $W_{10}=15 \text{ ms}^{-1}$ (~ 30 knots) that for a JONSWAP spectrum results in a SWH of 5.5 m and a peak wave frequency of 0.8 Hz.

B. STATIC TILT AND OPTIMAL ATTACHMENT POINT

The initial float test of the prototype buoy demonstrated the importance of decoupling the roll and heave motions. This is accomplished by attaching the mooring line at CG. In the force balance, the reactive force of the attachment is then equal to the sum of the wind and ocean current forces that are nearly the same due to the density ratio of air to water and the velocity ratio of water to wind (Figure 9). However, in the moment balance, the attachment moment is decoupled.

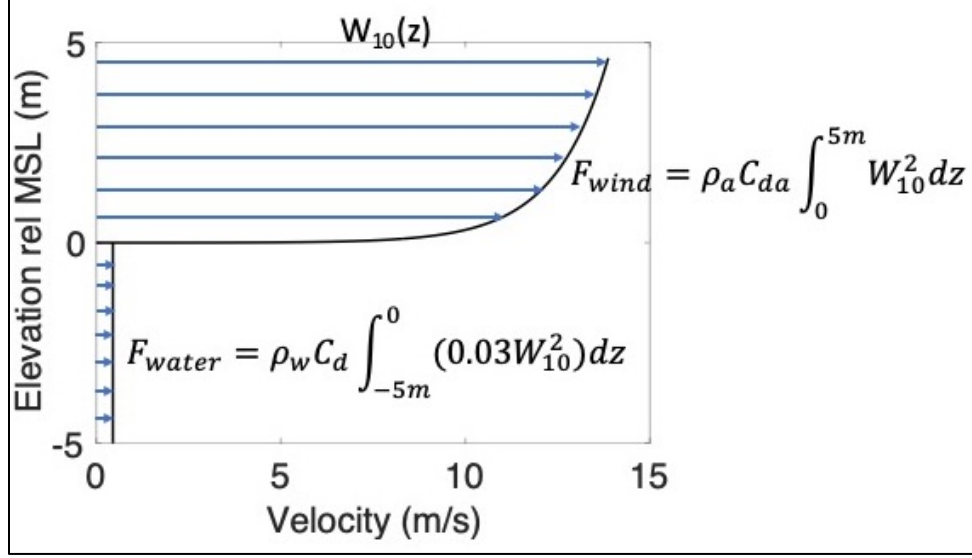


Figure 9. Schematic of wind and ocean current profiles. Logarithmic wind profile based on W_{10} wind at 10 m elevation and linear current profile, $U=0.03W_{10}$. Parameter values $C_d=1.0$ and $C_{da}=1.0$.

The mean tilt of the buoy (θ_{tilt}) is solved by the moment equation,

$$mgGB\theta_{tilt} = \int_0^{5m} F_W(z)(z + CG)dz + \int_{-CG}^0 F_C(z)(z + CG)dz + \int_{-4m}^{-CG} F_C(z)(z + CG)dz. \quad (23)$$

The tilt of the bouy (Figure 10) is determine by the force of the wind on the subaerial portion of the buoy (Figure 10a) plus the force of the water on the subaqueous portion from MSL to CG (Figure 10b). This is opposed by the force of the water on the subaqueous portion from CG to the bottom of the buoy (Figure 10c). The fins on the ballast/damping module were created specifically to increase the surface area of the bottom assembly to increase the opposing force and prevent rotation.

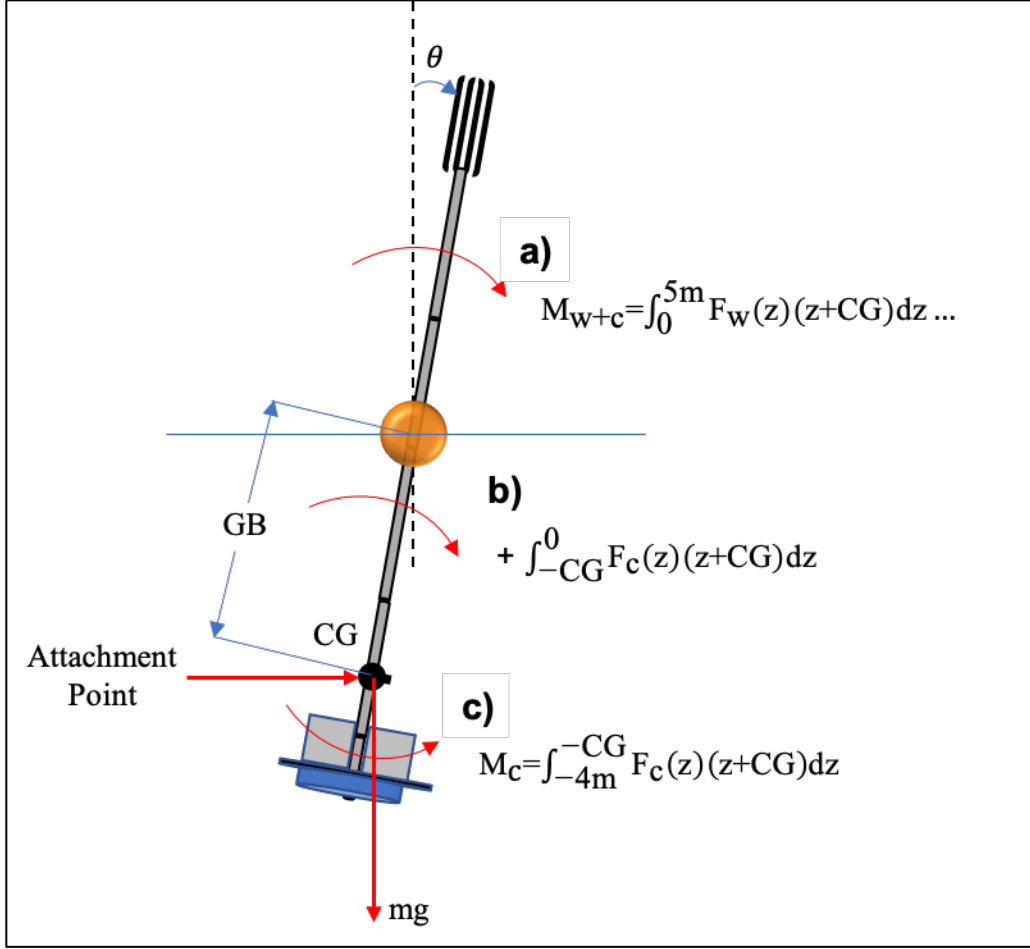


Figure 10. Tilt of the buoy due to wind forces and ocean current forces with moments about CG. The wind force (F_w) creates a positive tilt (a). The wave force (F_c) above CG creates a positive tilt (b) whereas the wave force below CG creates a negative tilt (c).

C. SPECTRAL WAVE FORCING

The dynamics of buoy are forced by waves described by linear wave theory, where the surface elevation is given by,

$$\eta(x,t) = A(f)e^{i(kx-\omega t)}, \quad (24)$$

and velocity terms by

$$u(x,z,t) = A(f)\omega H_u(z)e^{i(kx-\omega t)}$$

$$\dot{u}(x,z,t) = -iA(f)\omega^2 H_u(z)e^{i(kx-\omega t)}$$

$$w(x,z,t) = -iA(f)\omega H_w(z)e^{i(kx-\omega t)}$$

$$\dot{w}(x,z,t) = -A(f)\omega^2 H_w(z)e^{i(kx-\omega t)}$$

$$p(x,t) = \rho g(\eta(x,t)H_p(f) - z), \quad (25)$$

where u , w are the horizontal and vertical velocities, x is the horizontal distance travelled by the wave, ω is the angular frequency or $2\pi f$, z is the change in sea surface height, k is the wave number, $A(f)$ is the wave amplitude and the vertical variation of the wave velocity transfer functions are given by

$$H_u(z) = \frac{\cosh k(h+z)}{\sinh kh}, \quad (26)$$

and

$$H_w(z) = \frac{\sinh k(h+z)}{\sinh kh}, \quad (27)$$

and

$$H_p(z) = \frac{\cosh k(h+z)}{\cosh kh}, \quad (28)$$

where z is positive upward from MSL and h is the water depth. The objective is to solve for the heave spectrum of the buoy based on the surface wave spectrum approximated by

$$S_\eta(f) \simeq \frac{2A(f)^2}{\Delta f}, \quad (29)$$

where the heave spectrum is given by

$$S_Y(f) \simeq \frac{2Y(f)^2}{\Delta f}. \quad (30)$$

D. HEAVE DYNAMICS OF BUOY

The equation for heave motion of the buoy ($m_a=F$) for vertical variation $z(x, t)$, is given by

$$m_a \ddot{z} + B \dot{z} + k_s z = F_\eta(t) + F_D(t) + F_P(t) + F_I(t), \quad (31)$$

where m_a is the mass of the buoy, B is the damping parameter and $k_s = \rho g A_B$, is the so-called spring coefficient. $F_\eta(t)$, $F_D(t)$, $F_P(t)$, $F_I(t)$ is the forcing as a function of time for sea surface elevation, drag, pressure, and inertial forces, respectively.

The forcing terms are:

$$F_\eta(t) = \rho g A_B A(f) e^{i(kx - \omega t)}, \quad (32)$$

and

$$F_D(t) = \rho \frac{C_D}{2} A_D |w| w, \quad (33)$$

where A_B is the area of the buoyancy at the MSL, C_D is the drag coefficient and A_D is the area of the damping plate. A schematic of the buoy depicting the variables is shown in Figure 11. L_s is the height above MSL of the center of the anemometer transducers for wind observations and L_D is the depth below MSL of the damping plate on the ballast/damping assembly.

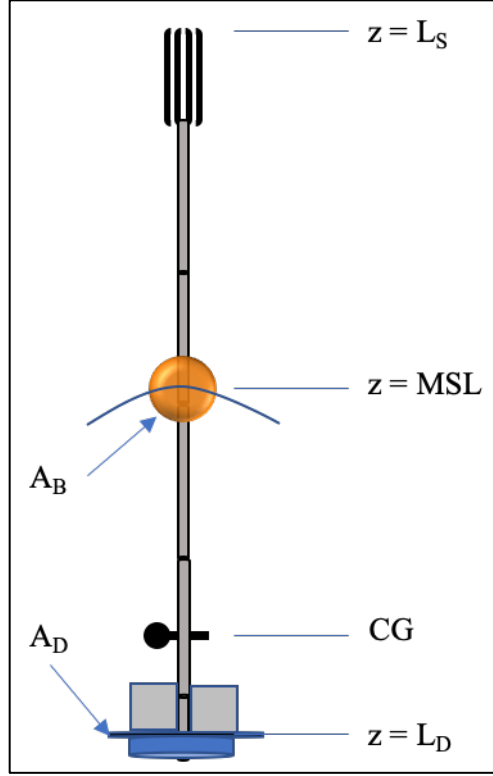


Figure 11. Schematic of buoy with variables defined for heave dynamics.

The velocity damping and wave forcing terms are of the form

$$F = \rho \frac{C_D}{2} |w|w, \quad (34)$$

which is nonlinear. The term is linearized by expanding in a Fourier series expansion and retaining the first term (Dean and Dalrymple, 1984):

$$|w|w \approx \frac{8}{3\pi} w_{\text{rms}} w, \quad (35)$$

where

$$w_{\text{rms}} = \left[\int_0^{f_{\text{max}}} S_w(f) df \right]^{\frac{1}{2}} = \left[\int_0^{f_{\text{max}}} |\omega H_w(f, h, z)|^2 S_\eta(f) df \right]^{\frac{1}{2}}, \quad (36)$$

then substituting into Equation (34) yields,

$$F_D(t) = \rho \frac{C_D}{2} \frac{8}{3\pi} A_D w_{rms} w = -i\omega D(f) A(f) e^{i(kx - \omega t)}, \quad (37)$$

where

$$D(f) = \rho \frac{4}{3\pi} C_D A_D w_{rms} H_w(f, h, z). \quad (38)$$

For the velocity damping term, since the buoy follows the waves, w_{rms} is the same for the entire buoy given by the surface value and Equation (36) simplifies to,

$$w_{rmsB} = \left[\int_0^{f_{max}} \omega^2 S_\eta(f) df \right]^{\frac{1}{2}}, \quad (39)$$

where

$$H_{rms} = \sqrt{8} \sigma_\eta, \quad (40)$$

then

$$B(f) = \rho \frac{4}{3\pi} C_D A_D w_{rmsB}. \quad (41)$$

The pressure force on the bottom of the buoyancy is

$$F_P(t) = A_b p(t) = P(f) A(f) e^{i(kx - \omega t)}, \quad (42)$$

where A_b is the area of the buoyancy, and $P(f) = \rho g A_b H_p(f)$.

The inertial wave forcing moment acting on the buoyancy

$$F_I(t) = \rho C_m A_b \int_{-L_D}^0 \dot{w} dz = -\omega^2 Q(f, z) A(f) e^{i(kx - \omega t)}, \quad (43)$$

where

$$Q(f,z) = \rho C_m A_b \int_{-L_D}^0 H_w(f,z) dz. \quad (44)$$

The solution of the buoy heave motion is assumed

$$z(x,t) = Y(f)e^{i(kx-\omega t)}$$

$$\dot{z}(x,t) = -i\omega Y(f)e^{i(kx-\omega t)}$$

$$\ddot{z}(x,t) = -\omega^2 Y(f)e^{i(kx-\omega t)}, \quad (45)$$

where $Y(f)$ is in general is complex allowing for phase shift between buoy and wave motions.

The vertical motion is calculated by substituting into Equation (31) to give

$$(-m\omega^2 - i\omega B + k_s)Y(f)e^{i(kx-\omega t)} = (k_s + P - i\omega D - \omega^2 Q)A(f)e^{i(kx-\omega t)}, \quad (46)$$

or

$$H_{\text{heave}}(f) = \frac{Y(f)}{A(f)} = \frac{(k_s + P - i\omega D - \omega^2 Q)}{(-m\omega^2 - i\omega B + k_s)} = |H_{\text{heave}}(f)|e^{i\varphi(f)}, \quad (47)$$

where $\varphi(f)$ is the phase difference between buoy heave motion and the waves.

The heave spectrum is given by

$$S_Y(f) = \frac{Y^2}{\Delta f} = |H_{\text{heave}}|^2 S_\eta(f), \quad (48)$$

and $\varphi(f)$ is the phase spectrum. The transfer function is dependent on the size of the damping plate. Figure 12 illustrates how the transfer function changes as the damping plate radius changes. A small damping plate would be underdamped, creating an unstable platform where response to high frequency waves would be exacerbated. A larger damping plate is adequately damped so there is less response to high frequency waves.

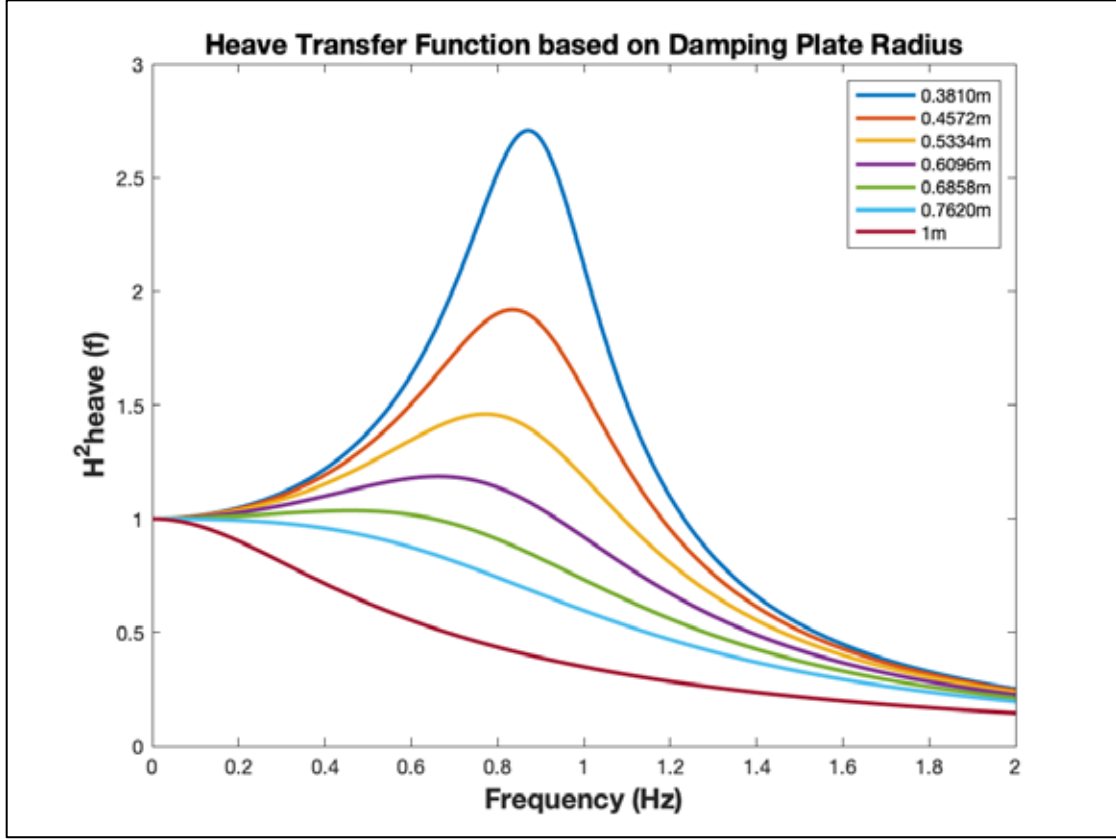


Figure 12. Heave transfer function based on damping plate radius. A heave transfer function value less than one means that the buoy response is damped at that frequency. A value greater than one means that the response would be magnified.

E. ROLL DYNAMICS OF BUOY

The equation for roll motion of the buoy is given by

$$I\ddot{\theta} + B\dot{\theta} + C\theta = M_I + M_D + M_R, \quad (49)$$

where I is the inertial damping moment, B is the velocity damping moment, C is the buoyancy damping moment, and θ is the rotation of the buoy about the CG, with positive rotation clockwise (Figure 13). M_I is the inertial wave forcing moment, M_D is the velocity wave forcing moment, and M_R is the disturbing moment owing to wave slope.

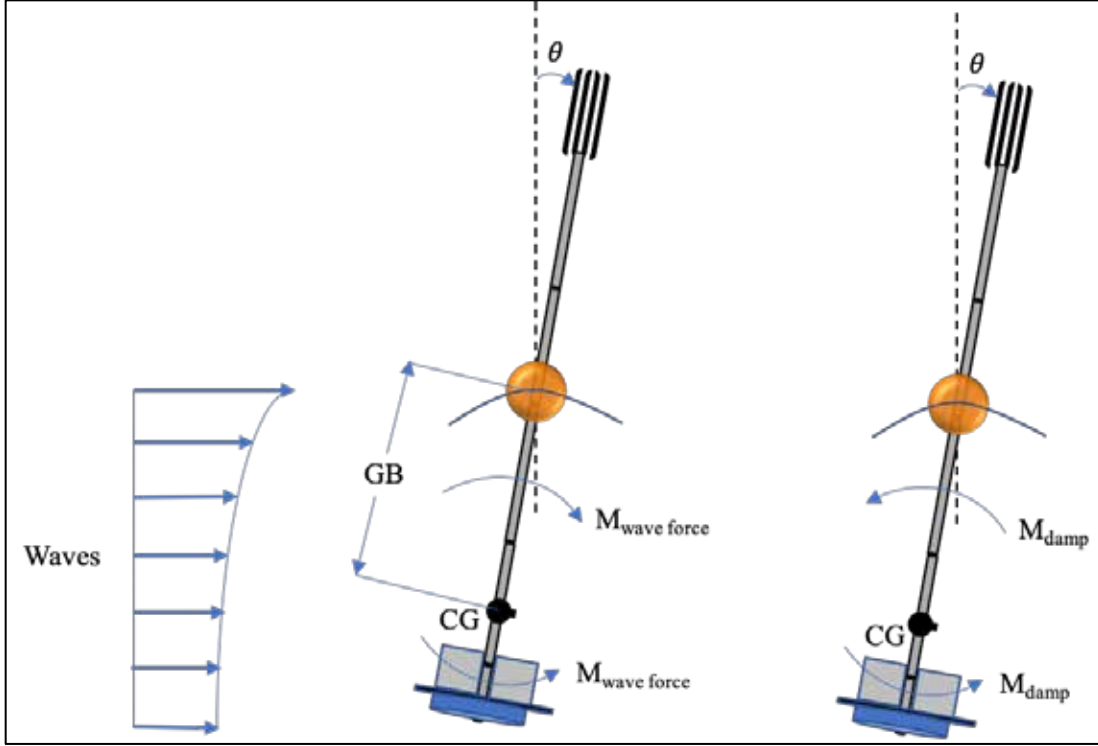


Figure 13. Buoy rotation due to wave forcing and damping motions. Moments for waves (left buoy) where the wave force above CG causes a positive rotation but the wave force below CG is negative. The moments for damping motions (right buoy) is negative above and below CG.

The inertial damping moment is given by,

$$I = \rho C_m \int_{-L}^0 z \frac{\pi}{4} d(z)^2 dz. \quad (50)$$

The velocity damping moment is,

$$\omega B = \rho \frac{C_D}{2} \frac{8}{3\pi} i\omega \bar{\theta} \int_{-L}^0 d(z) z^3 dz, \quad (51)$$

where the rotational velocity is,

$$\dot{\theta} = i\omega \theta \approx i\omega \frac{8}{3\pi} \bar{\theta}. \quad (52)$$

The buoyancy damping moment is

$$C = -gW_g GB. \quad (53)$$

where W_g is the dry weight of buoy and GB is the distance between the center of gravity and center buoyancy. The inertial wave forcing moment is given by,

$$M_I = \rho \frac{\pi}{4} C_m \int_{-L}^0 \dot{u} d(z)^2 dz = -i\omega^2 Q(z, f) A(f) e^{-i(kx - \omega t)}, \quad (54)$$

where,

$$Q(f) = \rho \frac{\pi}{4} C_m \int_{-L}^0 H_u(f, h) d(z)^2 dz. \quad (55)$$

The velocity wave forcing moment is,

$$M_D = \rho \frac{C_D}{2} \int_{-L}^0 |u| u d(z) dz = \omega^2 D(z, f) A(f) e^{-i(kx - \omega t)}, \quad (56)$$

where,

$$D(f) = \rho \frac{C_D}{2} \frac{4}{3\pi} H_{rms} \int_{-L}^0 H_u(f, h)^2 d(z) dz, \quad (57)$$

and where C_m is the inertial coefficient including added mass, C_D is the drag coefficient, and $d(z)$ is the diameter of the buoy as a function of elevation.

The disturbing moment owing to wave slope is

$$M_R = ik_s C A(f) e^{i(kx - \omega t)}, \quad (58)$$

however, since the buoy follows the surface, this term is neglected.

The velocity damping and wave forcing terms are of the form $|u|u$, which is nonlinear. Similar to the process in Section IV.D, the term is linearized by expanding in a Fourier series expansion and retaining the first term (Dean and Dalrymple, 1984):

$$|u|u \approx \frac{8}{3\pi} u_{\text{rms}} u, \quad (59)$$

where,

$$u_{\text{rms}}(f, z) = \frac{H_{\text{rms}}}{2} H_u(f, z), \quad (60)$$

so, the linear approximation is,

$$|u|u = \frac{4}{3\pi} H_{\text{rms}} H_u(f, h)^2. \quad (61)$$

The solution for the buoy rotation described in Equation (49) is given by

$$\theta(x, t) = \Theta(f) e^{i(kx - \omega t)}, \quad (62)$$

where $\Theta(f)$ is complex. The natural frequency of oscillation is found by setting the forcing and damping to zero and substituting the solution

$$(i^2 \omega^2 I + C) \Theta(f) e^{i(kx - \omega t)} = 0. \quad (63)$$

Substituting the solution into Equation (49), the response function of the buoy is given by

$$(-\omega^2 I - i\omega^2 B + C) \Theta(f) e^{i(kx - \omega t)} = (-i\omega^2 Q(z, f) + \omega^2 D(z, f) + ik_s C) A(f) e^{i(kx - \omega t)} \quad (64)$$

$$H_{\text{roll}}(f) = \frac{\Theta(f)}{A(f)} = \frac{(\omega^2 D - i\omega^2 Q + ik_s C)}{(C - \omega^2 I - i\omega^2 B)} = |H_{\text{roll}}(f)| e^{i\varphi(f)}, \quad (65)$$

where $\varphi(f)$ is the phase difference spectrum between buoy motion and the waves.

The roll spectrum is given by

$$S_{\text{roll}}(f) = |H_{\text{roll}}|^2 S_{\eta}(f), \quad (66)$$

where $S_{\eta}(f)$ is the wave spectrum.

The vertical distribution of the various terms in the roll dynamics equation at the peak frequency of 0.08 Hz are shown in Figure 14. The dominant moment term is due to wave velocity, which is positive above CG and negative below. The acceleration term is also positive above and negative below. Since they are opposing forces above and below CG the effect of roll will be minimized. The damping terms due to velocity and inertia are only negative, which is desired.

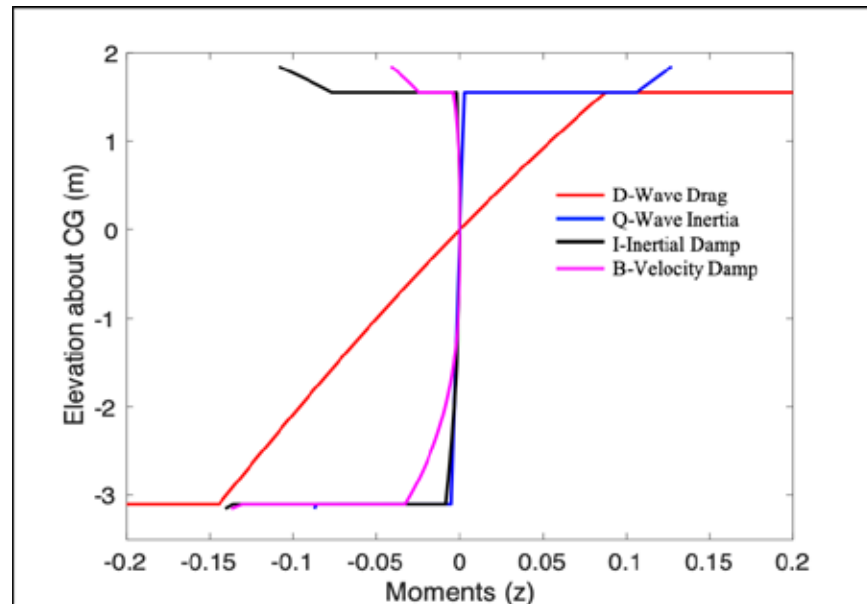


Figure 14. Plot of the distribution of the various moments in the roll dynamic equation over the vertical. The y-axis is the elevation in reference to the CG where negative is below CG and positive is above.

How the terms vary by frequency is shown in Figure 15. The roll impacts from the forcing and damping variables are minimal at low frequency and grow as wave frequency becomes greater than 0.15 Hz. At the higher frequency, the damping variables oppose the forcing variables indicating a stable system at these frequencies.

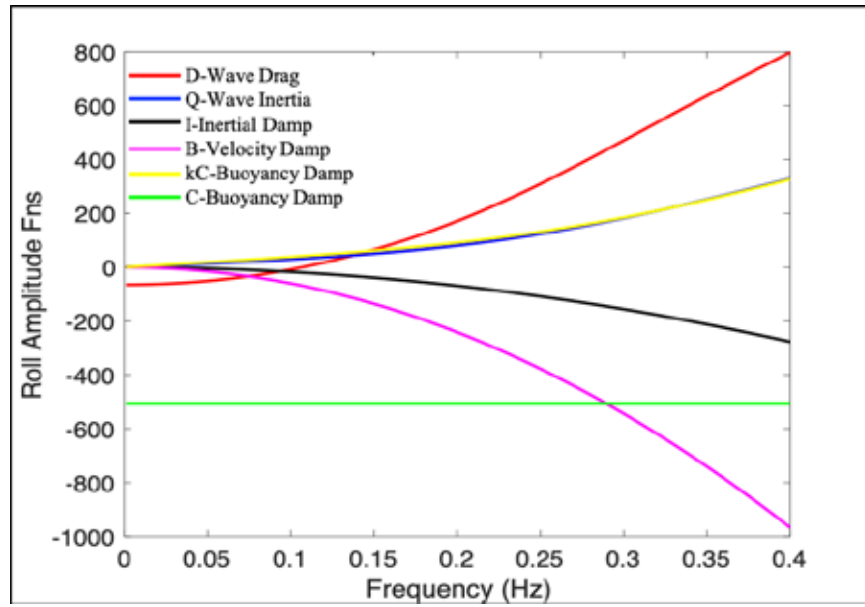


Figure 15. Plot of the variation of the various moments in the roll dynamic equation as a function of frequency.

V. DISCUSSION

A. STATIC TILT

As the buoy tilts over due to the steady wind, the elevation of the buoy above the water decreases, which changes the height of the air-sea interaction measurements. This also decreases the force on the buoy, which decreases the tilt. Therefore, it is necessary to iterate the tilt calculations. By averaging the tilts, the answer is obtained in about 7 iterations. To decrease the tilt, it is necessary to increase the CG by adding weight at the bottom. The more weight, the less the tilt. The tilt is also dependent on the length of buoy above and below water line. Table 1 are results calculated for 3 buoy lengths showing that the longer the subaqueous buoy length, the less the tilt in high winds. The static tilt of 25° for the 9 m length would result in observation being taken at 4.53 m above MSL. The 11 m length would result in the observations being taken at 4.78 m. Both results keep the measuring height above the 4 m wave boundary layer suggested by Edson et al. (2013). However, making the buoy longer also shifts the natural frequency of oscillation in roll towards lower frequencies, which opposes an initial dynamic design goal.

Table 1. Summary of results for $W_{10} = 15 \text{ ms}^{-1}$, $U=0$, $H_{\text{sig}}=5.5 \text{ m}$,
 $H_{\text{rms}} \approx H_{\text{heave}} \approx 4 \text{ m}$.

Buoy Length (m)	Subaqueous Buoy Length (m)	Tilt ($^\circ$)	Rms Roll ($^\circ$)	Natural f_{heave} (Hz)	Natural f_{roll} (Hz)	Fin Height (m)	CG from MSL (m)
9	4	20-25	5.6	0.92	0.49	0.483	2.65
10	5	15-19	5.6	0.90	0.45	0.559	3.35
11	6	11-17	5.8	0.91	0.40	0.635	4.03

B. HEAVE DYNAMICS

The heave dynamics of the buoy are determined by the wave forcing on the system. The heave dynamics are modified by changes in the sea surface elevation, drag, pressure, and inertial forces. Changes to the sea surface elevation and drag contribute the most to changes in heave so pressure and inertial forces were ignored. It is seen in Figure 11 that the size of the damping plate has a great effect on the heave response to the wave frequency. A larger damping plate would result in the desired response to only low frequency swell waves. However, making the damping plate overly large would become cumbersome to handle on a small boat, opposing an initial goal of being designed to deploy from a small boat.

For simulations, a JONSWAP wave spectrum (Figure 16 top) is applied for different wind speeds at 10 m elevation, W_{10} . An example for the upper limit of expected wind exposure, $W_{10} = 15 \text{ ms}^{-1}$, is shown in Figure 16. The SWH for this case is $H_s = 5.5 \text{ m}$. The heave response function (Figure 16 middle) for the 0.91 diameter damping plate shows the proper response to low frequency swell waves; however, its response becomes magnified from 0.4–0.9 Hz before becoming adequately damped. This result is undesired but will not be changed until field deployments confirm the modeling. The heave begins in-phase (Figure 17 bottom) with the waves and transitions to 180° out-of-phase at the mid-frequencies.

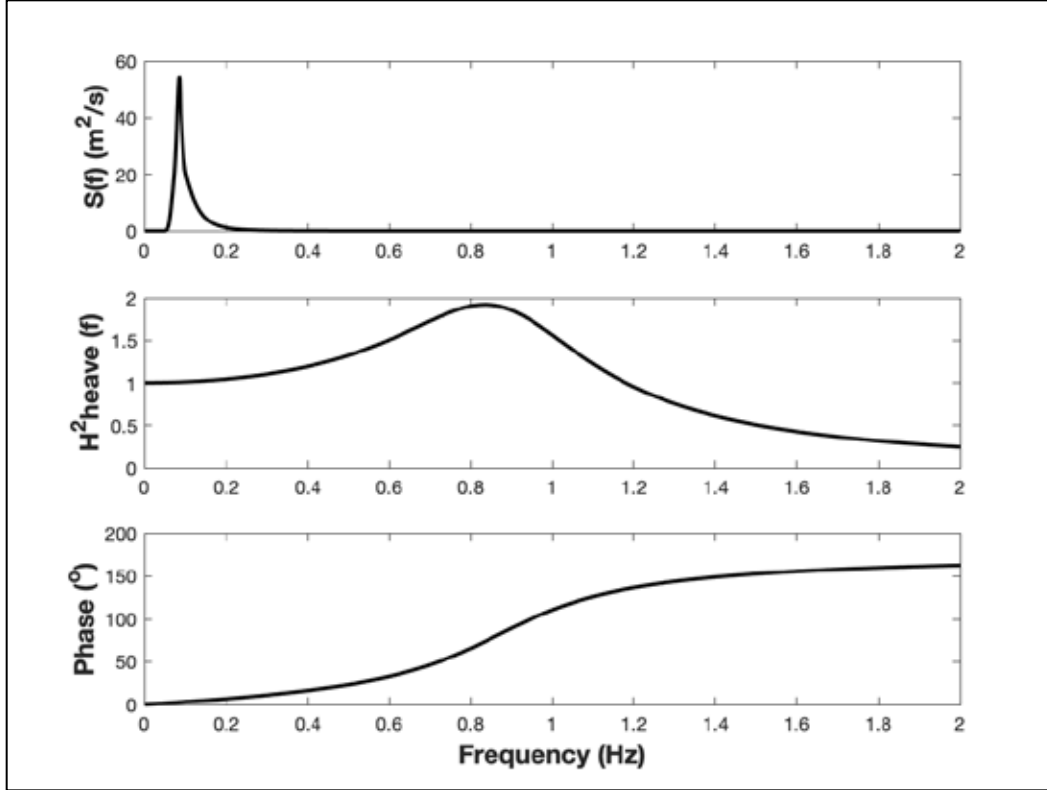


Figure 16. Plot of the heave response to wave interaction. The JONSWAP spectrum for $W_{10} = 15 \text{ ms}^{-1}$ (top), heave amplitude response function based on the 0.91 m damping plate (middle) and the phase difference between the heave of the buoy and the wave motion (bottom).

C. ROLL DYNAMICS

The roll dynamics are controlled by forcing from the wave velocities and accelerations, and damping by drag and inertial forces. It is seen in Figure 14 that the wave forcing moments about CG are (+) above and (-) below and that the wave velocities (and accelerations) are greater near the surface depending on frequency (lower frequencies are near uniform in shallow water compared with higher velocities near the surface for higher frequency). By moving the CG up or down, it is possible to have the wave velocity moments above and below the CG sum to zero, minimizing roll. This is a design objective. However, it is complicated as this depends on the velocity profile, which depends on the wave frequency and water depth. The CG is dependent on the distribution of weight over the vertical. Appendix C lists the components of the 11 m I-SPAR with its associated

weight and distance from MSL for reference. Any change to this distribution will change the CG and the roll dynamics of the buoy. It is noted that a bigger weight at the bottom does not necessarily result in a better design due to the inability to deploy from a small boat, which is the requirement to access the shoaling region.

For simulations, a JONSWAP wave spectrum (Figure 17 top) is applied for different wind speeds at 10 m elevation, W_{10} . An example for the upper limit of expected wind exposure, $W_{10} = 15 \text{ ms}^{-1}$, is shown in Figure 17. The significant wave height for this case is $H_s = 5.5 \text{ m}$. The roll response function (Figure 17 middle) shows no significant excitement to low frequency waves and grows slightly as the spectrum shifts towards high frequency waves. The roll begins in-phase (Figure 17 bottom) with the waves and shifts to 180° out-of-phase at 0.1 Hz , which corresponds to a 10 s wave period.

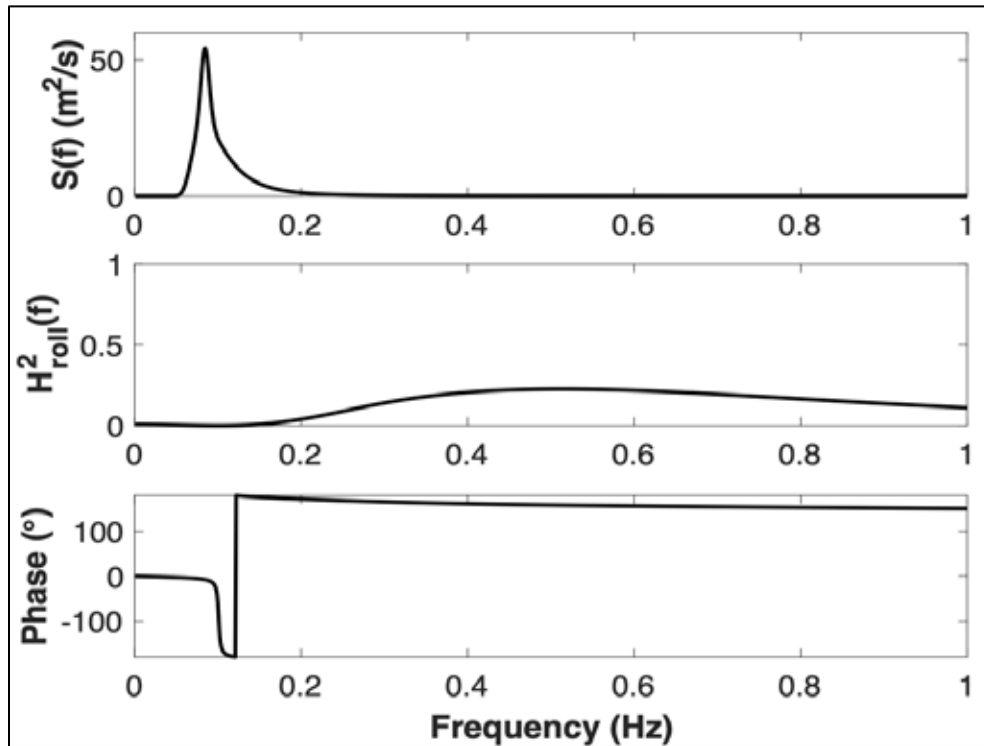


Figure 17. Plot of the roll response to wave interaction. The JONSWAP spectrum for $W_{10} = 15 \text{ ms}^{-1}$ (top), roll amplitude response function (middle) and the phase difference between the roll of the buoy and the wave motion (bottom).

VI. SUMMARY

A new, floating, air-sea, observational platform, referred to as the I-SPAR buoy, was developed for obtaining observations across the inner-shelf, which is the region where waves shoal. It is designed as a lightweight, modular system that can be deployed from a small boat to obtain measurements in shallow water, just seaward of the surf zone. The I-SPAR design was based on the height of observations, size and weight of the buoy, dynamical response to winds and waves, and ability to survive ocean conditions for several months. It required specific meteorological and motion sensors and a power module for 1–2 months deployments. Observations of wind turbulence need to be obtained at 5 m above the sea surface, which is suggested to be above the wave boundary layer. The subaqueous portion of the buoy needed to be as short as feasibly possible for shallow deployments, while keeping the overall weight to a minimum.

The I-SPAR is composed of five modules that were developed as a single, in-line, symmetric unit to reduce asymmetric wind drag. The electronics module contains a sonic anemometer, inertial motion unit (IMU), temperature/humidity (T/H) sensor, and a data acquisition system (DAS) necessary to synchronously obtain wind, buoy motions, and temperature/humidity observations at a fast sampling rate for accurately describing the wind stress and sensible heat flux. An iridium chip provides the capability to transmit real-time buoy monitoring, bulk statistics of wind, temperature, and humidity, and 5 min averaged flux calculations. The electronics are powered by the power module, a co-located solar panel rechargeable battery buoy. It provides unlimited power to the system at a 50% duty cycle.

Removing platform motion is a critical component for air-sea flux calculations from a floating platform. A GPS aided IMU with a dynamic pitch/roll accuracy of 0.03° is used to correct for platform motion. The IMU has an onboard EKF that fuses the low-frequency contributions of the accelerometer with the high-frequency contributions from the gyroscope to determine the Euler angle orientation of the buoy. The EKF sensor fusion alleviates the requirement of selecting an arbitrary cut-off frequency during data analysis that will under or overestimate the contributions in the mid-frequency, instead fusing the

contributions from both sensors. The GPS is used to correct for linear movement of the system. To accurately determine linear velocity, accelerometer measurements transformed from the time domain to the frequency domain through a DFFT. The integration in the frequency domain prevents phase shifts and any exaggeration of the inherent drift in accelerometer measurements.

The ballast/damping module comprises 59 kg of the buoy weight to keep the CG low for static and dynamic stability. The buoy is designed to follow the low frequency swell waves in the vertical heave motion. A damping plate located at the bottom of the buoy damps unwanted high frequency motions owing to wind waves. The dynamic vertical stability is determined by the size of the damping plate. The dynamic roll stability is determined by the forcing moments about the CG. Four vertical fins were attached to the damping plate to increase the subaqueous surface area for the dynamic restoring force below CG. The fins also provide rotational stability by preventing rotation during wave forcing. These features combine to make the buoy a stable platform for calculating air-sea fluxes. The 9 m I-SPAR is modeled to have a static tilt of $< 25^\circ$ and a root-mean-square dynamic roll of 5.6° in winds of 15 ms^{-1} with a SWH of 5.5 m. The 11 m I-SPAR is modeled to have a static tilt of $< 17^\circ$ and a root-mean-square dynamic roll of 5.8° in winds of 15 ms^{-1} with a SWH of 5.5 m.

The spar module contains the interconnected carbon fiber tubes capable of being built and transported in sections. This increases flexibility in shipping and allows the system to be deployed from a multitude of platforms. A buoyancy sphere provides the upward buoyancy force to offset the 84 kg and keep MSL at the center of the sphere. The mooring module keep the buoy anchored at a single location to obtain long-term measurements.

The I-SPAR final design has two lengths based on the subaqueous water depth limitations. The 9 m version of the buoy can be deployed in water depths as shallow as 7 m. The 11 m version is designed for deployment in water depths > 9 m. Due to restrictions, the final I-SPAR design was not able to be open-water tested during this period. As restrictions improve, the system will be water tested prior to field experimentation. The I-SPAR's first field experiment will consist of 10 systems deployed in 3 locations in

Monterey Bay, CA over a six-month period beginning in spring 2021. It will be paired with a few deeper water ASIS buoys as part of the Coastal Land Air-Sea Interaction (CLASI) field experiment.

THIS PAGE INTENTIONALLY LEFT BLANK

APPENDIX A

A few changes in the register setup were required for the VectorNav IMU to gain accurate measurements for a moored buoy application (VectorNav Technologies, personal communication). A hard/soft iron (HSI) calibration is recommended once the IMU is mounted in its full configuration. The calibration should be conducted away from any buildings or other objects that could create electromagnetic interference. This allows the IMU magnetometers to detect any interference from ferrous materials that can disrupt the magnetometer readings. The calibration is written to memory once the calibration is completed. The IMU also has the ability to conduct its own HSI calibration while operating in the field. This capability is important for a moving system, such as an unmanned aerial system, that has repeated interaction with external ferrous objects. However, for a moored, fixed location, buoy application, the HSI needs to be turned off so the IMU only utilizes the initial HSI conducted onshore prior to deployment. The heading for the IMU can be set to be absolute or relative. The absolute heading considers a static reference point for heading determination, and uses the accelerometers to describe the gravity orientation. The relative heading is used when the reference point is going to change over time during linear movements. For a moored buoy that is not drifting, the heading mode needs to be changed to absolute so that the observations can be transformed from a buoy frame of reference. The IMU with GPS further improves the slow frequency drift. With the GPS, magnetic declination models are provided onboard. The IMU has the ability for a user entered lat/long to determine location compared to true north. The VN-200 will update the position automatically once GPS fixes are obtained. The VN-100 requires the user to enter a position for the magnetic declination model. In order for this to occur, the world magnetic model and world gravity model needs to be enabled in the VNs. This provides a most accurate determination of the systems orientation.

THIS PAGE INTENTIONALLY LEFT BLANK

APPENDIX B

As shown in Figure 6, there are three different coordinate systems used in the IMU, anemometer, and the platform correction procedures outlined in Edson et al. (1998). The three axes must be aligned to prevent errors rotating from the platform coordinate system to ENU and removing platform motions. The following changes are required in the data processing code to align the three coordinate systems. The first steps are to align the anemometer wind observations to the Edson coordinate system. The U-wind observations from the anemometer needs to be aligned to the x-axis and to the positive direction in Edson where,

$$U_{OBS} = -V_{ANEMOMETER}. \quad (67)$$

The V-wind observations from the anemometer needs to be aligned to the y-axis of Edson where,

$$V_{OBS} = U_{ANEMOMETER}. \quad (68)$$

The positive directions for the IMU are positive to the bow, starboard, and down (Figure 6a). The coordinates need to be changed to align to Edson where positive is to the bow, port, and up (Figure 6b). The IMU y-axis acceleration observations need to be changed so that positive is to port where,

$$A_{OBS,Y} = -A_{IMU,Y}. \quad (69)$$

The IMU z-axis acceleration observations need to be changed so that positive is to up where,

$$A_{OBS,Z} = -A_{IMU,Z}. \quad (70)$$

Finally, the change in direction for positive vectors results in a change in positive angle rotations for the y-axis. The following changes ensures the positive rotations remain clockwise. The IMU rotational velocity observations needs to change so that a clockwise rotation is bow down where,

$$\Omega_{\text{OBS},Y} = -\Omega_{\text{IMU},Y}. \quad (71)$$

The IMU pitch orientation needs to change so that pitch is positive bow down where,

$$\theta = -\theta_{\text{IMU}}. \quad (72)$$

APPENDIX C

The dynamic pitch and roll of the buoy are determined by the moments about CG. The moments are determined by the distribution of weight along the buoy. Therefore, the weight distribution is critical to the dynamic performance of the buoy when exposed to high winds and seas. Table 2 lists all of the components of the buoy from the top to the bottom with their associated weight and elevation about MSL. A positive elevation is upward from MSL.

Table 2. I-SPAR components for 11 m with weight and distance from MSL.

Component	Weight (kg)	Elevation (m)
GPS Antenna	0.10	+5.12
Electronics Module	3.83	+4.14 to +5.12
Wire Lock Clamp	0.05	+3.99
Carbon Fiber Tube	1.85	+1.71 to +4.14
Wire Lock Clamp	0.05	+1.79
Carbon Fiber Tube Insert	0.43	+1.56 to +1.86
Carbon Fiber Tube	1.59	-0.38 to +1.71
Wire Lock Clamp	0.05	+1.64
Buoyancy Sphere Brace	0.17	+0.31
Buoyancy Sphere	11.34	0 (MSL)
Buoyancy Sphere Brace	0.17	-0.31
Bolt/Washer/Nut	0.02	-0.31
Carbon Fiber Tube Insert	0.43	-0.23 to -0.53
Bolt/Washer/Nut	0.02	-0.46
Bolt/Washer/Nut	0.02	-2.83
Carbon Fiber Tube Insert	0.43	-2.75 to -3.05
Carbon Fiber Tube	1.85	-0.38 to -2.81
Bolt/Washer/Nut	0.02	-2.98
CG Eyebolt and Smart Shackle	0.83	-4.03
Power Cable	0.30	-4.03 to +4.14
Bolt/Washer/Nut	0.02	-5.01
Carbon Fiber Tube Insert	0.43	-4.94 to -5.24
Carbon Fiber Tube	1.73	-2.81 to -5.09
Bolt/Washer/Nut	0.02	-5.16
Ballast/Damping Module	59.29	-5.09 to -6.00

THIS PAGE INTENTIONALLY LEFT BLANK

LIST OF REFERENCES

- Anctil, F., M. A. Donelan, W. M. Drennan, and H. C. Graber, 1994: Eddy-correlation measurements of air–sea fluxes from a discus buoy. *J. Atmos. Oceanic Technol.*, **11**, 1144–1150, [https://doi.org/10.1175/1520-0426\(1994\)011<1144:ECMOAS>2.0.CO;2](https://doi.org/10.1175/1520-0426(1994)011<1144:ECMOAS>2.0.CO;2).
- Baskutis, S., M. Nariūnas, and J. Baskutienė, 2014: The fiber volume fraction influence on mechanical properties of multi-layered carbon tubes. *Mech.*, **20**, 543–549, <https://doi.org/10.5755/j01.mech.20.6.8880>.
- Blomquist, B. W., B. J. Huebert, C. W. Fairall, L. Bariteau, J. B. Edson, J. E. Hare, and W. R. McGillis, 2014: Advances in air–sea CO₂ flux measurement by eddy correlation. *Bound.-Layer Meteor.*, **152**, 245–276, <https://doi.org/10.1007/s10546-014-9926-2>.
- Bourras, D., and Coauthors, 2014: A New Platform for the Determination of Air–Sea Fluxes (OCARINA): Overview and First Results. *J. Atmos. Oceanic Technol.*, **31**, 1043–1062, <https://doi.org/10.1175/JTECH-D-13-00055.1>.
- Bourras, D., and Coauthors, 2019: Air-sea turbulent fluxes from a wave-following platform during six experiments at sea. *J. Geophys. Res. Oceans*, **124**, 4290–4321, <https://doi.org/10.1029/2018JC014803>.
- Brandt, A. and R. Brincker, 2014: Integrating time signals in frequency domain – Comparison with time domain integration. *Measurement*, **58**, 511–519, <https://doi.org/10.1016/j.measurement.2014.09.004>.
- Brigante, C. M. N., N. Abbate, A. Basile, A. C. Faulisi and S. Sessa, 2011: Towards miniaturization of a MEMS-based wearable motion capture system. *IEEE Trans. Ind. Electron.*, **58**, 3234–3241, <https://doi.org/10.1109/TIE.2011.2148671>.
- Campbell Scientific, 2019: CR6 Specifications. Accessed 06 October 2020, https://s.campbellsci.com/documents/us/product-brochures/s_cr6.pdf.
- Chalikov, D. V. and S. Rainchik, 2011: Coupled numerical modeling of wind and waves and the theory of the wave boundary layer. *Bound.-Layer Meteor.*, **138**, 1–41, <https://doi.org/10.1007/s10546-010-9543-7>.
- Chen, S., F. Qiao, C. J. Huang, and B. Zhao, 2018: Deviation of wind stress from wind direction under low wind conditions. *J. Geophys. Res. Oceans*, **123**, 9357–9368, <https://doi.org/10.1029/2018JC014137>.

- Chen, S., F. Qiao, W. Jiang, J. Guo, and D. Dai, 2019: Impact of Surface Waves on Wind Stress under Low to Moderate Wind Conditions. *J. Phys. Oceanogr.*, **49**, 2017–2028, <https://doi.org/10.1175/JPO-D-18-0266.1>.
- Cronin M. F., and Coauthors, 2019: Air-sea fluxes with a focus on heat and momentum. *Front. Mar. Sci.* **6**, 430, <https://doi.org/10.3389/fmars.2019.00430>.
- Dean, R. G., and R. A. Dalrymple, 1984: *Water wave mechanics for engineers and scientists*, Prentice Hall Inc, 353 pp.
- Donelan, M. A., W. M. Drennan, and K. B. Katsaros, 1997: The air–sea momentum flux in conditions of mixed wind sea and swell. *J. Phys. Oceanogr.*, **27**, 2087–2099, [https://doi.org/10.1175/1520-0485\(1997\)027<2087:TASMF1>2.0.CO;2](https://doi.org/10.1175/1520-0485(1997)027<2087:TASMF1>2.0.CO;2).
- Drennan, W. M., M. A. Donelan, E. A. Terray, and K. B. Katsaros, 1996: Oceanic turbulence dissipation measurements in SWADE. *J. Phys. Oceanogr.*, **26**, 808–815, [https://doi.org/10.1175/1520-0485\(1996\)026<0808:OTDMIS>2.0.CO;2](https://doi.org/10.1175/1520-0485(1996)026<0808:OTDMIS>2.0.CO;2).
- Drennan, W. M., H. C. Graber, D. Hauser, and C. Quentin, 2003: On the wave age dependence of wind stress over pure wind seas. *J. Geophys. Res.*, **108**, 8062, <https://doi.org/10.1029/2000JC000715>.
- Drennan, W. M., H. C. Graber, C. O. Collins III, A. Herrera, H. Potter, R. J. Ramos, and N. J. Williams, 2014: EASI: An air–sea interaction buoy for high winds. *J. Atmos. Oceanic Technol.*, **31**, 1397–1409, <https://doi.org/10.1175/JTECH-D-13-00201.1>.
- Edson, J. B., A. A. Hinton, K. E. Prada, J. E. Hare, and C. W. Fairall, 1998: Direct covariance flux estimates from mobile platforms at sea. *J. Atmos. Oceanic Technol.*, **15**, 547–562. [https://doi.org/10.1175/1520-0426\(1998\)015<0547:DCFEFM>2.0.CO;2](https://doi.org/10.1175/1520-0426(1998)015<0547:DCFEFM>2.0.CO;2).
- Edson, J. B. and Coauthors, 2013: On the exchange of momentum over the open ocean. *J. Phys. Oceanogr.*, **43**, 1589–1610, <https://doi.org/10.1175/JPO-D-12-0173.1>.
- Finnigan, J. J., R. Clement, Y. Malhi, R. Leuning, and H. A. Cleugh, 2003: Re-evaluation of long-term flux measurement techniques. Part I: Averaging and coordinate rotation, *Boundary-Layer Meteor.*, **107**, 1–48, <https://doi.org/10.1023/A:1021554900225>.
- Fisher, F. H., and F. N. Spiess, 1963: Flip-floating instrument platform. *J. Acoust. Soc. Amer.*, **35**, 1633–1644, <https://doi.org/10.1121/1.1918772>.
- Flügge, M., M. B. Paskyabi, J. Reuder, J. B. Edson, and A. J. Plueddemann, 2016: Comparison of Direct Covariance Flux Measurements from an Offshore Tower and a Buoy. *J. Atmos. Oceanic Technol.*, **33**, 873–890, <https://doi.org/10.1175/JTECH-D-15-0109.1>.

- Flügge, M., M. Bakhoday-Paskyabi, J. Reuder, O. El Guernaoui, 2019: Wind Stress in the Coastal Zone: Observations from a Buoy in Southwestern Norway. *Atmosphere*, **10**, 491, <https://doi.org/10.3390/atmos10090491>.
- Geernaert, G. L., F. Hansen, M. Courtney, and T. Herbers, 1993: Directional attributes of the ocean surface wind stress vector. *J. Geophys. Res.*, **98**, 16 571–16 582. <https://doi.org/10.1029/93JC01439>.
- Graber, H. C., E. A. Terray, M. A. Donelan, W. M. Drennan, J. Van Leer, and D. B. Peters, 2000: ASIS—A new air-sea interaction spar buoy: Design and performance at sea, *J. Atmos. Oceanic Technol.*, **17**, 708–720, [https://doi.org/10.1175/1520-0426\(2000\)017<0708>AANASI.2.0.CO;2](https://doi.org/10.1175/1520-0426(2000)017<0708>AANASI.2.0.CO;2).
- Grachev, A. A., and C. W. Fairall, 2001: Upward momentum transfer in the marine boundary layer. *J. Phys. Oceanogr.*, **31**, 1698–1711, [https://doi.org/10.1175/1520-0485\(2001\)031<1698:UMTITM>2.0.CO;2](https://doi.org/10.1175/1520-0485(2001)031<1698:UMTITM>2.0.CO;2).
- Grachev, A. A., C. W. Fairall, J. E. Hare, J. B. Edson, and S. D. Miller, 2003: Wind stress vector over ocean waves. *J. Phys. Oceanogr.*, **33**, 2408–2429. [https://doi.org/10.1175/15200485\(2003\)033<2408:WSVOOW>2.0.CO;2](https://doi.org/10.1175/15200485(2003)033<2408:WSVOOW>2.0.CO;2).
- Grachev, A. A., L. S. Leo, H. J. S. Fernando, C. W. Fairall, E. Creegan, B. W. Blomquist, A. J. Christman, and C. M. Hocut, 2017: Air sea/land interaction in the coastal zone. *Bound.-Layer Meteor.*, **167**, 181–210, <https://doi.org/10.1007/s10546-017-0326-2>.
- Hare, J. E., C. W. Fairall, W. R. McGillis, J. B. Edson, B. Ward, and R. Wanninkhof, 2004: Evaluation of the National Oceanic and Atmospheric Administration/Coupled-Ocean Atmospheric Response Experiment (NOAA/COARE) air-sea gas transfer parameterization using GasEx data. *J. Geophys. Res.: Oceans*, **109**, <https://doi.org/10.1029/2003JC001831>.
- Högström, U., E. Sahleé, A. S. Smedman, A. Rutgersson, E. Nilsson, K. K. Kahma, and W. M. Drennan, 2015: Surface stress over the ocean in swell-dominated conditions during moderate winds. *J. Atmos. Sci.*, **75**, 2579–2587. <https://doi.org/10.1175/JAS-D-17-0334.1>.
- Kahma, K. K., M. A. Donelan, W. M. Drennan, and E. A. Terray, 2016: Evidence of energy and momentum flux from swell to wind. *J. Phys. Oceanogr.*, **46**, 2143–2156, <https://doi.org/10.1175/JPO-D-15-0213.1>.
- Kaimal, J. C., and D. A. Haugen, 1969: Some errors in the measurement of Reynolds stress. *J. Appl. Meteor.*, **8**, 460–462, [https://doi.org/10.1175/1520-0450\(1969\)008<0460:SEITMO>2.0.CO;2](https://doi.org/10.1175/1520-0450(1969)008<0460:SEITMO>2.0.CO;2).

- Islam, T., M. S. Islam, M. Shajid-Ul-Mahmud, and M. Hossam-E-Haider, 2017: Comparison of complementary and Kalman filter based data fusion for attitude heading reference system. *AIP Conf. Proc.*, **1919**, 020002, <https://doi.org/10.1063/1.5018520>
- Łuczak, S., R. Grepl, and M. Bodnicki, 2017: Selection of MEMS accelerometers for tilt measurements. *J. Sens.*, **2017**, 1–14, <https://doi.org/10.1155/2017/9796146>.
- Mahrt, L., D. Vickers, J. Howell, J. Hojstrup, J. M. Wilczak, J. Edson, and J. Hare, 1996: Sea surface drag coefficients in the Risø Air Sea Experiment. *J. Geophys. Res.*, **101**, 14327–14335, <https://doi.org/10.1029/96JC00748>.
- Mauder, M and M. J. Zeeman, 2018: Field intercomparison of prevailing sonic anemometers. *Atmos. Meas. Tech.*, **11**, 249–263, <https://doi.org/10.5194/amt-11-249-2018>.
- McGillis, W. R., J. B. Edson, J. E. Hare, and C. W. Fairall, 2001: Direct covariance air-sea CO₂ fluxes. *J. Geophys. Res.*, **106**, 16729–16745, <https://doi.org/10.1029/2000JC000506>.
- Miller, S. D., T. S. Hristov, J. B. Edson, and C. A. Friehe, 2008: Platform motion effects on measurements of turbulence and air-sea exchange over the open ocean. *J. Atmos. Ocean. Technol.*, **25**, 1683–1694. <https://doi.org/10.1175/2008JTECHO547.1> ^[1] _{SEP}
- Oost, W. A., C. W. Fairall, J. B. Edson, S. D. Smith, R. J. Anderson, J. A. B. Wills, K. B. Katsaros, and J. DeCosmo, 1994: Flow Distortion Calculations and their Application in HEXMAX, *J. Atmos. Oceanic Technol.*, **11**, 366–386. [https://doi.org/10.1175/1520-0426\(1994\)011<0366:FDCATA>2.0.CO;2](https://doi.org/10.1175/1520-0426(1994)011<0366:FDCATA>2.0.CO;2).
- Ortiz-Suslow, D. G., B. K. Haus, N. J. Williams, N. J. M. Laxague, A. J. H. M. Reniers, and H. C. Graber, 2015: The spatial-temporal variability of air-sea momentum fluxes observed at a tidal inlet, *J. Geophys. Res.: Oceans*, **120**, 660–676, <https://doi.org/10.1002/2014JC010412>.
- Ortiz-Suslow, D. G., B. K. Haus, N. J. Williams, H. C. Graber, and J. H. MacMahan, 2018: Observations of air-sea momentum flux variability across the inner shelf. *J. Geophys. Res.: Oceans*, **123**, 8970–8993, <https://doi.org/10.1029/2018JC014348>.
- R.M. Young Company, 2006: Ultrasonic Anemometer Model 81000 Manual. Accessed 08 October 2020, [http://www.youngusa.com/Manuals/81000-90\(I\).pdf](http://www.youngusa.com/Manuals/81000-90(I).pdf).
- Raghukumar, K., G. Chang, F. Spada, C. Jones, T. Janssen, and A. Gans, 2019: Performance Characteristics of “Spotter,” a Newly Developed Real-Time Wave Measurement Buoy. *J. Atmos. Oceanic Technol.*, **36**, 1127–1141, <https://doi.org/10.1175/JTECH-D-18-0151.1>.

- Rieder, K. F., J. A. Smith, and R. A. Weller, 1994: Observed directional characteristics of the wind, wind stress and surface waves on the open ocean. *J. Geophys. Res.*, **99**, 22589–22596, <https://doi.org/10.1029/94JC02215>.
- Rotronic AD, 2019: Rotronic HC2A Data Sheet. Accessed 07 October 2020, <https://www.rotronic.com/en-us/humidity-measurement-feuchtemessung-temperaturmessung/humidity-measurement-feuchte-messung/probes-hygroclip2-fuehler/hc2-s/hc2a-s3.html>.
- Sabatini, A. M., 2011: Kalman-Filter-Based Orientation Determination Using Inertial/Magnetic Sensors: Observability Analysis and Performance Evaluation. *Sensors*, **11**, 9182–9206, <https://doi.org/10.3390/s111009182>.
- Sahleé, E., W. M. Drennan, H. Potter and M. A. Rebozo, 2012: Waves and air-sea fluxes from a drifting ASIS buoy during the Southern Ocean Gas Exchange experiment. *J. Phys. Oceanogr.*, **10**, 18, <https://doi.org/10.1029/2012JC008032>.
- Semedo, A., Ø. Saetra, A. Rutgersson, K. K. Kahma, and H. Pettersson, 2009: Wave-induced wind in the marine boundary layer. *J. Atmos. Sci.*, **66**, 2256–2271. <https://doi.org/10.1175/2009JAS3018.1>.
- Shabani, B., A. V. Babanin, and T. E. Baldock, 2016: Observations of the directional distribution of the wind energy input function over swell waves. *J. Geophys. Res.: Oceans*, **121**, 1174–1193. <https://doi.org/10.1002/2015JC011225>.
- Shaeffer, D. K., 2013: Mems inertial sensors: A tutorial overview. *IEEE Commun. Mag.*, **51**, 100–109, <https://doi.org/10.1109/MCOM.2013.6495768>.
- Smith, S. D., C. W. Fairall, G. L. Geernaert, and L. Hasse, 1996: Air-sea fluxes: 25 years of progress. *Boundary-Layer Meteor.*, **78**, 247–290, <https://doi.org/10.1007/BF00120938>.
- Thornton, E. B., and R. T. Guza, 1983: Transformation of wave height distribution. *J. Geophys. Res.*, **88**, 5925–5938, <https://doi.org/10.1029/JC088iC10p05925>.
- VectorNav Technologies, 2020: Product Brochure. Accessed 02 October 2020, https://www.vectornav.com/docs/default-source/product-brochures/vectornav-product-brochure.pdf?sfvrsn=59877a0_9.
- Villas Bôas A. B., and Coauthors, 2019: Integrated observations of global surface winds, currents, and waves: requirements and challenges for the next decade. *Front. Mar. Sci.*, **6**, 425, <https://doi.org/10.3389/fmars.2019.00425>.
- Welch, G. F., 2009: History: The Use of the Kalman Filter for Human Motion Tracking in Virtual Reality. *Presence-Teleoperators And Virtual Environ.*, **18**, 72–91, <https://doi.org/10.1162/pres.18.1.72>.

- Weller, R. A., S. P. Bigorre, J. Lord, J. D. Ware, and J. B. Edson, 2012: A surface mooring for air–sea interaction research in the Gulf Stream. Part I: Mooring design and instrumentation. *J. Atmos. Oceanic Technol.*, **29**, 1363–1376, <https://doi.org/10.1175/JTECH-D-12-00060.1>.
- Wilczak, J., S. Oncley, and S. Stage, 2001: Sonic anemometer tilt correction algorithms. *Boundary-Layer Meteor.*, **99**, 127–150, <https://doi.org/10.1023/A:1018966204465>.
- Zhang, D., and Coauthors, 2019: Comparing Air-Sea Flux Measurements from a New Unmanned Surface Vehicle and Proven Platforms During the SPURS-2 Field Campaign. *Oceanography*, **32**, 122–133, <https://doi.org/10.5670/oceanog.2019.220>.
- Zhang, F. W., W. M. Drennan, B. K. Haus, and H. C. Graber, 2009: On wind-wave-current interactions during the Shoaling Waves Experiment. *J. Geophys. Res.: Oceans*, **114**, <https://doi.org/10.1029/2008JC004998>.
- Zhao, Z. K., C. X. Liu, Q. Li, G. F. Dai, Q. T. Song, and W. H. Lv, 2015: Typhoon air-sea drag coefficient in coastal regions. *J. Geophys. Res.: Oceans*, **120**, 716–727, <https://doi.org/10.1002/2014JC010283>.

INITIAL DISTRIBUTION LIST

1. Defense Technical Information Center
Ft. Belvoir, Virginia
2. Dudley Knox Library
Naval Postgraduate School
Monterey, California